


Streaming-potential-mediated pressure-driven transport of Phan-Thien–Tanner fluids in a microchannel

Sandip Sarkar **Department of Mechanical Engineering, Jadavpur University, Kolkata 700 032, India*

(Received 5 December 2019; revised manuscript received 25 March 2020; accepted 20 April 2020; published 18 May 2020)

Streaming potential mediated pressure driven electrokinetic transport of Phan-Thien–Tanner fluids in a slit type parallel plate microchannel is studied analytically and semianalytically. Without adopting the traditional considerations of Debye–Hückel linearization approximation for low surface potentials, exact analytical solutions are obtained for the electrostatic potential distribution, velocity, and volumetric flow rates taking into account the full Poisson-Boltzmann equation. The influences of interfacial electrokinetics and viscoelasticity on the streaming potential development, polymeric stress components, shear viscosity, and the hydroelectric energy conversion efficiency are incorporated concurrently. Major findings indicate that the magnitude of the induced streaming potential, volumetric flow rates, and the energy conversion efficiency increases up to a threshold limit of zeta potential of $\zeta \leq 6$, however, it follows an asymptotic reduction at the other end of higher zeta potentials $6 < \zeta \leq 10$. The polymeric stress components and shear viscosity follow a similar trend in the regime of $1 \leq \zeta \leq 10$, which is primarily governed by the streaming potential field. In contrast, the transverse averaged shear viscosity in the range $1 \leq \zeta \leq 10$ obeys an opposite trend by yielding an inverted parabolic shape. Amplification in the Stern layer conductivity yields a progressive reduction in the streaming potential magnitude and the hydroelectric energy conversion efficiency. The effect of the fluid viscoelasticity designated by the Weissenberg number exhibits a linear enhancement in streaming potential, flow rates, and the energy conversion efficiency. Moreover, we show that with the optimal combinations of surface charging and fluid viscoelasticity, it is possible to accomplish a giant augmentation in the hydroelectric energy conversion efficiency and flow rates. The analytical and semianalytical results presented in this investigation are believed to be worthy not only to cater deeper understanding in micro- and nanofluidic transport characteristics but also will act as functional design instrument for the future generation of energy efficient narrow fluidic devices.

DOI: [10.1103/PhysRevE.101.053104](https://doi.org/10.1103/PhysRevE.101.053104)

I. INTRODUCTION

Electrokinetic mediation evolves from a charged substrate in contact with an ionic fluid. Subjected to an applied pressure gradient, when an ionic solution is pushed through a microchannel, the excess counterions within the mobile part of the electric double layer (EDL) dragged in tune with the flow direction [1,2]. This essentially brings about the preferential accumulation of the ions towards the downstream end of the channel and thus generating an electric field, namely, the streaming current [2,3]. The overall consequence may induce an electric voltage gradient across the two ends of the channel in order to balance the streaming current, termed as the streaming potential. The streaming current holds the competence to propel an extraneous electrical load resistor and therefore harvesting electrical energy from such narrow fluidic devices [4]. In this context, it may be noted here that the formation of EDL enables this hydroelectrical energy conversion mechanism. The EDL develops owing to the acquirement of net charge distribution by the channel walls in contact with the aqueous solution by the adsorption or dissociation

chemical reactions [2,5]. This wall charge is equalized by the free oppositely charged ions in the liquid, which get disseminated in a layer of wall-cohering fluid thereby giving rise to a net charge distribution in the vicinity of the bonding substrate [6].

In consequence of the high surface to volume ratio of micro- or nanofluidic devices, the faster developments in micro- or nanochannel fabrication technologies bring additional thrust into the evergrowing possibilities of rendering the physical concepts into real-life applications [7]. Such applications include recent developments in laboratory-on-a-chip (LOC) devices, microelectromechanical systems (MEMS), DNA hybridization [8,9], *in situ* drug delivery module, micrototal analysis systems (μ TAS), peristaltic micropumps [10,11], mass flow controller [12], lab on a CD (LabCD), to name a few [13–15]. Accordingly, several experimental, numerical, and theoretical research attempts have been made by various research groups across the globe to understand this intriguing phenomenon. Notably, the condition gets extensively occupied with a probable mundane interaction among flow rheology and fluid kinematics. In this perspective, it is recognized that biological fluids, such as blood, protein solutions, saliva, DNA solutions, synovial fluid, or various biofluids carrying long-chain molecular arrangements

*thesandipsarkar3@gmail.com

exhibit viscoelastic behaviors [16–24]. One group of many researchers, Afonso *et al.* [25], carried out theoretical investigation on electro-osmotic flows (EOFs) employing various non-Newtonian fluid models, namely FENE-P (finitely extensible nonlinear elastic model-Peterlin's approximation) and linear PTT (Phan-Thien–Tanner) [25–30]. Of late, Ferrás *et al.* [31] presented closed-form analytical or semianalytical solutions for EOFs with a simplified PTT model with linear, quadratic, or exponential kernel for the stress coefficient function, the Giesekus model, and the Johnson-Segalman model [31]. There have been few other reported works on EOFs with non-Newtonian fluids, where the inelastic behavior is characterized by the Ostwald–de Waele power-law model [32–34].

While various types of interplay among EOFs and associated electrohydrodynamic phenomena fall under the wide-ranging arena of electrokinetics [35–43], in this study, we primarily focus on the consequences of streaming potential followed by the electrohydrodynamic energy conversion efficiency. Such electrokinetic flow of viscoelastic fluids, incorporating the topics of streaming potential, streaming current, and the concept of hydroelectrical energy conversion, received much research attention over the recent past [44–48]. A fundamental characteristic of such systems is the occurrence of separate existence over microscales. Perhaps the energy harnessed from a solo microchannel is minute; however, one may achieve significantly higher in magnitude by employing arrays of macroscopic nanoporous or nanopores materials [49–51]. Nevertheless, by manipulating the interactions between complicated rheology of viscoelastic fluids and interfacial electrokinetics, one may achieve higher energy conversion efficiency [6]. It is worthy of mentioning here that this energy-harvesting mechanism with viscoelastic fluids holds the futuristic potential of constructing green-energy recovery plants or energizing miniscule devices for biomedical applications. For a linearized Maxwell fluid with an oscillatory driving pressure gradient, a giant augmentation in the energy conversion efficiency has been reported recently [6]. On the other hand, for non-Newtonian power-law obeying fluids, dramatic improvement in the streaming potential and the energy transfer efficiency is observed with an additional influence of steric (size effect of the ionic species) interactions [5]. Likewise, wall substrate in the Cassie-Baxter state occurs in superhydrophobic surfaces, revealed to induce a considerable amplification in the streaming potential [52–56]. A comprehensive review of the electrokinetic transport of viscoelastic fluids may be found elsewhere [57,58]. Albeit a handful of research studies have been addressed in the literature to highlight the consequences of non-Newtonian fluid rheology on streaming potential and energy conversion efficiency in a microchannel, hitherto, the corresponding body of knowledge for PTT fluid has yet to emerge in the literature. Nevertheless, contemporary research exploiting non-Newtonian fluids in a microchannel reveals that one may enhance streaming potential and energy conversion efficiency through high-frequency pressure pulsations [3]. A later study on the implications of solvent rheology and confinement on ionic conductivity in non-Newtonian fluids found that shear thinning behavior promotes an improved magnitude of the streaming potential at lower low ionic concentrations [59].

Recently, the streaming potential and electrokinetic energy conversion efficiency of viscoelastic fluid has been analyzed in a polyelectrolyte-grafted narrow fluidic channel [60]. The reported results indicate higher energy conversion efficiency of a soft narrow channel than those for a rigid channel as the forcing frequency of the driving pressure gradient moves away from the resonant frequency regime. The effect of asymmetric wall zeta potentials for the streaming potential development of the power-law obeying fluid in a slit type microchannel has been studied of late [61]. The theoretical calculations yield stronger dependency of the streaming potential on the asymmetry of the zeta potential for shear-thinning fluids [61].

Although the influence of applied electric field on the transport characteristics (EOFs) of PTT fluid is well studied in the contemporary literature [41,62], the streaming potential mediated pressure-driven transport characteristics of PTT fluids in a microchannel is not yet understood. From the viewpoint of biotechnological applications, the knowledge of the rheological behavior of biofluids is of prime importance. The differential viscoelastic equations characterizing such biological fluids encompassing their memory effects, rheological characteristics, normal stress differences, and shear-thinning viscosity may be accommodated in the PTT fluid constitutive model equations [25–31]. Thus, the analytic solutions are helpful not just to explain the physics at the ready but also to advance the field of the existing body of knowledge in the scientific community. Motivated from these interests, in this work, we address a theoretical analysis of streaming potential mediated pressure-driven flow of PTT fluids in a slit type parallel plate microchannel. Without limiting the classical considerations of thin EDLs and low surface potential, in the present research, we employ the full scale analytical solution of the Poisson-Boltzmann equation to attain potential distribution inside the flow domain. We derived closed-form analytical solutions for the electrostatic potential, velocity, and volumetric flow rate. We also obtain an abridged solution based on the celebrated Debye–Hückel approximation in an aim to aid numerical imminence of the influences of this estimation on the flow attributes. Besides, the pertinent research questions that we are trying to address in this study are as follows: What is the mechanism by which the streaming potential field induced during pressure-driven transport of PTT fluid gets affected by the interfacial electrokinetics and fluid rheological parameters? How does the hydrodynamic field become affected by the interfacial electrokinetics? What is the consequence of fluid rheological parameters on the flow field? Do the interfacial electrokinetics and fluid rheological parameters affect the polymeric stress components? What about corresponding consequences on the shear viscosity? What is the percentage of energy that can be harnessed by utilizing this induced streaming potential field? How does this hydroelectrical energy conversion efficiency get influenced by the interfacial electrokinetics and fluid rheological parameters? Finally, can we find an optimal parametric regime for which the hydroelectrical energy conversion efficiency is maximum?

The remainder of this paper is organized as follows: In Sec. II, we describe the physical system and formulate the problem mathematically. We next present the constitutive relationships of the PTT fluids for the pressure-driven streaming

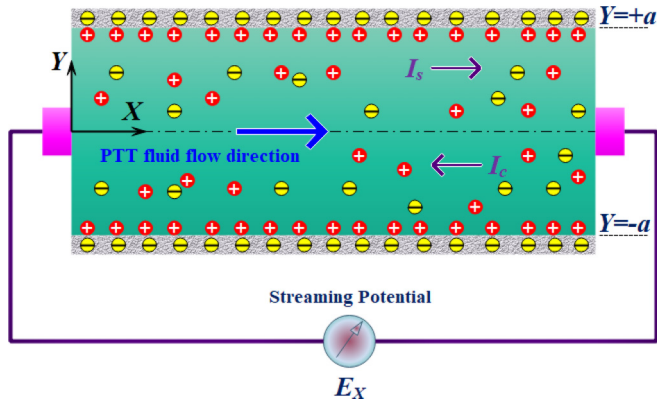


FIG. 1. Schematic of the flow geometry under consideration. Fluid motion is actuated by the applied pressure gradient along the positive X direction, which causes the development of induced streaming potential field E_X . I_s and I_c are the induced streaming and conduction currents, respectively.

potential mediated flows and derived analytical solutions for the velocity and volumetric flow rates. In Sec. III, we demonstrate detailed implications of the interfacial electrokinetics and the governing electrohydrodynamic parameters on the streaming potential development, velocity, flow rate, and hydroelectrical energy conversion efficiency. In the end, in Sec. IV, we draw key concluding remarks from the study.

II. MODEL FORMULATION

We consider the pressure driven flow of a non-Newtonian ionic fluid modeled as the PTT viscoelastic fluid through a slit-type parallel plate microchannel of separation $2a$. The lateral width of the channel is W , and longitudinal length L , where $L, W \gg 2a$. The origin is located at the centerline of the channel, where the coordinate axis X runs along the streamwise direction and Y sweeps vertically upwards. Figure 1 illustrates a schematic of the flow geometry under consideration. The fluid motion is set towards the X direction of the channel by the imposed pressure gradient along the same direction. The fluid comprises a $z : z$ symmetric electrolyte with an electrical permittivity of the solution ϵ . In consequence of the formation of EDL at the substrate walls, we assume that the walls of the channel carry a uniform electrical potential at the walls (wall zeta potential) ζ^* [1]. In spite of the absence of applied electric field, in the crosswise direction of the channel, a back-streaming potential field E_X , known as the streaming potential, is implicitly induced through a competing advection-electromigration mechanism in the mobile part of the EDL [56]. We further consider noninterference of EDLs from the walls of the channel thereby invoking a situation of thin EDL approximation. The flow is assumed to be steady, unidirectional, and incompressible. In addition, in the present study, we have assumed temperature independent constant thermophysical properties of the fluid.

A. Electrostatic potential distribution

The development of the EDLs near charged surfaces brings about an electrostatic potential (Ψ) distribution inside the

EDL. This induced EDL potential Ψ obeys the Poisson-Boltzmann equation, and may be expressed as [1]

$$\nabla^2 \Psi = -\frac{\rho_e}{\epsilon}. \quad (1)$$

For fully developed, steady, unidirectional flow with thin and nonoverlapped EDLs, as assumed in the present analysis, Eq. (1) transforms into [1]

$$\frac{d^2 \Psi}{dY^2} = -\frac{\rho_e}{\epsilon}. \quad (2)$$

In Eq. (2), ρ_e is the net charge density distribution. For constant permittivity fluid and neglecting the steric effect (point charges of ionic species), one may obtain the expression for ρ_e by the Boltzmann distribution [1],

$$\rho_e = -2n_0 e z \sinh\left(\frac{e z \Psi}{k_B T}\right). \quad (3)$$

Here, n_0 is the bulk ionic concentration ($n_0 = C_A N_A$, where, C_A is the molar ionic concentration, N_A being Avogadro's number, 6.023×10^{23}), e is the protonic charge ($1.602 \times 10^{-19} C$), k_B is the Boltzmann constant ($1.381 \times 10^{-23} m^2 kg s^{-2} K^{-1}$), T is the absolute temperature, and z is the valence of the ionic species [2]. It is worth mentioning that considerations of the finite size of the ionic species (steric effect) and its implications on the electrokinetic transport characteristics of the PTT fluids are discussed in Appendix A.

We employ Eqs. (2) and (3) to yield the celebrated Poisson-Boltzmann equation,

$$\frac{d^2 \Psi}{dY^2} = \bar{\kappa}^2 \sinh\left(\frac{e z \Psi}{k_B T}\right), \quad (4)$$

where $1/\bar{\kappa}^2 = \epsilon k_B T / 2n_0 e^2 z^2$ is the Debye length, a characteristic parameter for the EDL thickness [1]. Equation (4) is subjected to the following set of boundary conditions: $[d\Psi/dY]_{Y=0} = 0$ and $[\Psi]_{Y=a} = \zeta^*$ [4]. In an effort to obtain an analytical solution governing EDL potential distribution, we integrate Eq. (4) subjected to the boundary conditions, as discussed, to yield the EDL potential distribution in dimensionless form [4,56]:

$$\psi = 4 \tanh^{-1}[\exp\{-\kappa(1-y)\} \tanh(\zeta/4)]. \quad (5)$$

In order to obtain the dimensionless form of EDL potential distribution, as given in Eq. (5), we have introduced the following dimensionless quantities as relevant to the present investigation [4,56]: $\psi = e z \Psi / k_B T$, $y = Y/a$, $\zeta = e z \zeta^* / k_B T$, and $\kappa = a \bar{\kappa}$.

Alternatively, for lower values of zeta potentials ($|\zeta^*| < 26$ mV) one may invoke the Debye-Hückel linearization approximation to obtain a simplified expression for ψ , which reads [56]

$$\psi = \zeta \{\cosh(\kappa y) / \cosh(\kappa)\}. \quad (6)$$

B. Governing fluid flow equations

In the present investigation, the continuity and momentum equations constitute governing transport equations for the fluid motion. Accordingly, for the streaming potential mediated pressure driven fully developed flow of incompressible

viscoelastic fluid, the continuity and the Cauchy's momentum equations including the body force term are given by [31,37,38,63–65]

$$\nabla \cdot \vec{U} = 0, \quad (7a)$$

$$\rho \frac{D\vec{U}}{Dt} = -\nabla p + \nabla \cdot \boldsymbol{\tau} + \eta_{\text{eff}} \nabla^2 \vec{U} + \vec{F}_E, \quad (7b)$$

where \vec{U} is the velocity vector, ρ is the density of fluid, t is the time, p is the pressure, $\boldsymbol{\tau}$ is the extra-stress tensor as attributable to the polymeric contribution, and η_{eff} is the Newtonian solvent viscosity [37,38]. In the present research, we assume that in comparison with the polymeric contribution, the solvent viscosity is negligible, thus, $\eta_{\text{eff}} = 0$. A detailed analysis of the streaming potential mediated hydrodynamic characteristics of PTT fluids with the contribution of the solvent viscosity ($\eta_{\text{eff}} \neq 0$) is given in Appendix B. The source term \vec{F}_E appearing in the momentum equation, Eq. (7b), is the body force term per unit volume stemming from electrokinetic influences, in consequence of the development of the streaming potential field. The expression for \vec{F}_E is [1]

$$\vec{F}_E = \rho_e E, \quad (8)$$

where E is the streaming potential field.

C. Constitutive equations for the PTT model

As mentioned in the preceding discussion, in this work, we have employed the simplified Phan-Thien–Tanner (sPTT) model to describe the rheological behavior of the viscoelastic fluid. Therefore, by adopting the sPTT constitutive relationships, the polymeric extra-stress tensor $\boldsymbol{\tau}$ can be expressed in a compact generic equation as [25,31]

$$f(\text{tr}\boldsymbol{\tau})\boldsymbol{\tau} + \lambda \bar{\boldsymbol{\tau}} = 2\eta \mathbf{D}, \quad (9)$$

where $f(\text{tr}\boldsymbol{\tau})$ is the scalar function representing the trace of the polymeric extra-stress tensor $\boldsymbol{\tau}$, λ is the fluid relaxation time, η is the polymeric viscosity coefficient, $\mathbf{D} = (\nabla \vec{U} + \nabla \vec{U}^T)/2$ is the tensor denoting rate of deformation, and $\bar{\boldsymbol{\tau}}$ designates the Gordon-Schowalter convective derivative of the stress tensor $\boldsymbol{\tau}$, which reads [25,31]

$$\bar{\boldsymbol{\tau}} = \frac{D\boldsymbol{\tau}}{Dt} - (\nabla \vec{U}^T \cdot \boldsymbol{\tau} + \boldsymbol{\tau} \cdot \nabla \vec{U}) \quad (10)$$

For the sPTT model, the stress coefficient function $f(\text{tr}\boldsymbol{\tau})$ takes the following form [25,31]:

$$f(\text{tr}\boldsymbol{\tau}) = 1 + \frac{\varepsilon_s \lambda}{\eta} \tau_{kk}. \quad (11)$$

In Eq. (11), ε_s is the extensibility parameter of the model and is responsible for limiting the fluid extensional viscosity, with $\tau_{kk} = \tau_{XX} + \tau_{YY} + \tau_{ZZ}$ being the trace of the extra-stress tensor. It may be noted here that for dilute polymeric solutions, the Johnson-Segalman constitutive equation [$f(\tau_{kk}) = 1$] can be obtained by putting $\varepsilon_s = 0$ [25,31].

We now invoke the assumptions of fully developed, two dimensional ($\tau_{ZZ} = 0$), unidirectional flow, for which $\vec{U} \equiv$

$\{U(Y), 0, 0\}$. With these considerations, Eq. (9) can be reduced to the following form:

$$f(\tau_{XX} + \tau_{YY})\tau_{XX} = 2\lambda \left(\frac{dU}{dY} \right) \tau_{XY}, \quad (12)$$

$$f(\tau_{XX} + \tau_{YY})\tau_{YY} = 0, \quad (13)$$

$$f(\tau_{XX} + \tau_{YY})\tau_{XY} = (\eta + \lambda \tau_{YY}) \left(\frac{dU}{dY} \right). \quad (14)$$

Therefore, from Eq. (13), we can write $\tau_{YY} = 0$ and thus $\tau_{kk} = \tau_{XX}$. We now divide Eq. (12) by Eq. (14) to obtain the following relation among shear and normal stresses [31]: $\tau_{XX} = 2(\lambda/\eta)\tau_{XY}^2$. After some simplifications of Eqs. (11)–(14), we finally get the following equation for the shear stress:

$$\tau_{XY} + \frac{2\varepsilon_s \lambda^2}{\eta^2} (\tau_{XY})^3 = \eta \left(\frac{dU}{dY} \right). \quad (15)$$

D. Closed form analytical solution for the velocity

In the present investigation, we invoked the assumptions of steady, incompressible, fully developed microchannel flow. Therefore, under these conditions, the Cauchy's momentum equations, Eq. (7), leads to [31]

$$\frac{d\tau_{XY}}{dY} = \frac{dp}{dX} + \varepsilon E_X \frac{d^2\Psi}{dY^2}, \quad (16)$$

where dp/dX is the pressure gradient along the streamwise direction and E_X is the induced streaming potential field. We employ a symmetric condition at the channel centerline and for a nonoverlapping EDL, $[\tau_{XY}, \Psi]_{Y=0} = 0$, Eq. (16) can be integrated once to obtain [31]

$$\tau_{XY} = \left(\frac{dp}{dX} \right) Y + \varepsilon E_X \frac{d\Psi}{dY}. \quad (17)$$

Substituting Eq. (17) into Eq. (15), we get an explicit equation for the flow velocity gradient inside the microchannel as

$$\frac{dU}{dY} = \frac{1}{\eta} \left[\left(\frac{dp}{dX} \right) Y + \varepsilon E_X \frac{d\Psi}{dY} \right] + \frac{2\varepsilon_s \lambda^2}{\eta^3} \left[\left(\frac{dp}{dX} \right) Y + \varepsilon E_X \frac{d\Psi}{dY} \right]^3. \quad (18)$$

To examine the dynamics further, we first nondimensionalize the relevant equation, Eq. (18), in the following way [45–47]: the dimensionless velocity, $u = U/U_{\text{ref}}$, where $U_{\text{ref}} = -(a^2/\eta)(dp/dX)$ is the reference velocity scale, $E = E_X/E_{\text{ref}}$ is the dimensionless streaming potential, and $E_{\text{ref}} = -(a^2/\varepsilon \xi^*)(dp/dX)$ being the scale for reference streaming potential. With the above nondimensionalization scheme, we can write the dimensionless form of Eq. (18) as

$$\frac{du}{dy} = \left(\frac{E}{\xi} \frac{d\psi}{dy} - y \right) + \frac{2\varepsilon_s \text{Wi}_k^2}{\kappa^2} \left(\frac{E}{\xi} \frac{d\psi}{dy} - y \right)^3. \quad (19)$$

In Eq. (19), Wi_k is the Weissenberg number based on reference velocity scale, is defined as $\text{Wi}_k = \lambda \bar{\kappa} U_{\text{ref}} = \lambda \kappa U_{\text{ref}}/a$.

In an aim to obtain a closed-form analytical solution for the velocity distribution $u(y)$, we impose the following set of dimensionless boundary conditions as pertinent to Eq. (19)

[31]: we apply symmetry boundary conditions at the channel centerline, whereas no-slip boundary condition for the velocity is applied at the top ($y = +1$) and bottom ($y = -1$)

walls, $u(y)|_{y=\pm 1} = 0$. Upon imposing the preceding boundary conditions, Eq. (19) can be integrated to obtain an analytical formula for velocity distribution of the form

$$\begin{aligned}
 u(y) = & \frac{24\varepsilon_s \text{Wi}_k^2 E}{\zeta \kappa^4} [\text{Li}_3\{pe^{\kappa(y-1)}\} - \text{Li}_3\{-pe^{\kappa(y-1)}\} + \text{Li}_3(-p) - \text{Li}_3(p)] \\
 & + \frac{24\varepsilon_s \text{Wi}_k^2 E}{\zeta \kappa^3} [y\text{Li}_2\{-pe^{\kappa(y-1)}\} - y\text{Li}_2\{pe^{\kappa(y-1)}\} + \text{Li}_2(p) - \text{Li}_2(-p)] \\
 & - \frac{24\varepsilon_s \text{Wi}_k^2 E^2}{\zeta^2 \kappa^2} \left[\ln\left(\frac{e^{2\kappa} - p^2 e^{2\kappa y}}{e^{2\kappa} - p^2}\right) - \frac{\zeta y^2}{2E} \ln\left\{\frac{1 + pe^{\kappa(y-1)}}{1 - pe^{\kappa(y-1)}}\right\} - \frac{\zeta}{2E} \ln\left(\frac{1-p}{1+p}\right) \right] + \frac{\varepsilon_s \text{Wi}_k^2}{2\kappa^2} (1 - y^4) \\
 & + 16\varepsilon_s \text{Wi}_k^2 p \left(\frac{E}{\zeta}\right)^3 \left[\frac{e^{\kappa(y+1)}}{p^2 e^{2\kappa y} - e^{2\kappa}} + \frac{2e^{\kappa(y+3)}}{(e^{2\kappa} - p^2 e^{2\kappa y})^2} - \frac{3y \zeta e^{2\kappa}}{pE\kappa(e^{2\kappa} - p^2 e^{2\kappa y})} + \frac{3\zeta}{pE\kappa(1 - p^2)} \right] \\
 & - \frac{48\varepsilon_s \text{Wi}_k^2 E^2}{\zeta^2 \kappa} (1 - y) - \frac{16\varepsilon_s \text{Wi}_k^2 p E^3 (1 + p^2)}{\zeta^3 (1 - p^2)^2} + \frac{16\varepsilon_s \text{Wi}_k^2 E^3}{\zeta^3} [\tanh^{-1}(p) - \tanh^{-1}\{pe^{\kappa(y-1)}\}] \\
 & + \frac{4E}{\zeta} [\tanh^{-1}\{pe^{\kappa(y-1)}\} - \tanh^{-1}(p)] + \frac{1}{2}(1 - y^2). \tag{20}
 \end{aligned}$$

Here, $p = \tanh(\zeta/4)$. The Jonquière’s function or the polylogarithm $\text{Li}_s(\beta)$ of order s and argument β is defined by a power series, $\text{Li}_s(\beta) = \sum_{r=1}^{\infty} \frac{\beta^r}{r^s}$.

On the other hand, invoking the assumptions for the Debye–Hückel linearization approximation, as given in Eq. (6) for the dimensionless EDL potential distribution, we obtain the following velocity profile:

$$\begin{aligned}
 u(y) = & \frac{3}{8\kappa^4 \cosh^2(\kappa)} [\varepsilon_s \text{Wi}_k^2 \{4\kappa^4 E^2 (E + y^2 - 1) - \kappa^2 (E^2 + 12E + y^4 - 1) - 24E\} - \kappa^4 (2E + y^2 - 1)] \\
 & - \frac{\cosh(3\kappa)}{24\kappa^4 \cosh^3(\kappa)} [\varepsilon_s \text{Wi}_k^2 \{4\kappa^4 E^3 + 3\kappa^2 (3E^2 + 12E + y^4 - 1) + 72E\} + 3\kappa^4 (2E + y^2 - 1)] \\
 & + \frac{E}{24\kappa^4 \cosh^3(\kappa)} [4\varepsilon_s \text{Wi}_k^2 \kappa^4 E^2 \cosh(3\kappa y) + 18\varepsilon_s \text{Wi}_k^2 \kappa^2 E \{\cosh(2\kappa y) - 2\kappa y \sinh(2\kappa y)\} \cosh(\kappa) \\
 & + 36\varepsilon_s \text{Wi}_k^2 \kappa^2 y^2 \cosh(\kappa y + 2\kappa) + 12\{\varepsilon_s \text{Wi}_k^2 (-3\kappa^4 E^2 + 6\kappa^2 y^2 + 12) + \kappa^4\} \cosh(\kappa y) \\
 & + 6\{6\varepsilon_s \text{Wi}_k^2 (2 + \kappa^2 y^2) + \kappa^4\} \cosh(\kappa y - 2\kappa) \\
 & - 144\varepsilon_s \text{Wi}_k^2 \kappa y \cosh(2\kappa) \sinh(\kappa y) - 144\varepsilon_s \text{Wi}_k^2 \kappa y \sinh(\kappa y) + 72\varepsilon_s \text{Wi}_k^2 \cosh(\kappa y + 2\kappa) \\
 & + 18\varepsilon_s \text{Wi}_k^2 \kappa (4 + \kappa^2 E) \{\sinh(\kappa) + \sinh(3\kappa)\} + 6\kappa^4 \cosh(\kappa y + 2\kappa)]. \tag{21}
 \end{aligned}$$

At this juncture, it is important to note that the dimensionless streaming potential field E , appearing in Eqs. (20) and (21), is an unknown parameter and can be evaluated by employing the condition of electroneutrality of current.

E. Streaming potential and the Hydroelectric energy conversion efficiency

The estimation of the streaming potential field is based on the concept of the electroneutrality principle. It states that at each cross section of the channel, the pressure-driven flow induces a streaming current owing to the downstream motion of the ions that must be counterpoised by the sum total of the conduction currents as a consequence of electromigration along the bulk and the stern layer. The aforesaid physical statement can be expressed mathematically in a dimensional form as [1]

$$\int_{-a}^a z e (n_+ - n_-) U(Y) dY + \frac{z^2 e^2 E_X}{f} \int_{-a}^a (n_+ + n_-) dY + 2 \sigma_{\text{stern}} E_X = 0. \tag{22}$$

The first term in Eq. (22) denotes the streaming current, the second term represents the conduction current flowing through the “mobile” fluid layers, whereas the conduction current passing through the “immobilized” stern layer is represented by the last term [56]. Here, $f = 2 n_0 e^2 z^2 / \sigma_B$ is the ionic friction factor, σ_{stern} is the stern layer conductivity, and σ_B is the bulk ionic conductivity [1]. The number densities of the positive (n_+) and negative (n_-) ions are given by the Boltzmann distribution, $n_{\pm} = n_0 \exp(\mp e z \Psi / k_B T)$ [1].

In a dimensionless form, Eq. (22) can be written in the form

$$\int_0^1 u(y) \sinh(\psi) dy - \frac{\alpha E}{\zeta} \left[\int_0^1 \cosh(\psi) dy + Du \right] = 0, \tag{23}$$

where $Du = \sigma_{\text{stern}}/a\sigma_B$ is the Dukhin number and $\alpha = \eta\sigma_B/2\epsilon n_0(k_B T)$ is a nondimensional conductivity parameter [1].

We see that Eq. (23) formally puts a closure on the intricacy of finding out the velocity distribution. Nevertheless, we notice that Eq. (23) is an implicit equation in E , since the velocity $u(y)$ has a functional dependence with E . Therefore, we employ an iterative technique to obtain the solution for E and $u(y)$. Towards this, we start by assuming a guess value of E to find out the velocity profile as expressed in Eq. (20). We, then, use this velocity distribution to obtain an estimation of E from Eq. (23). Using this current estimation of E , we again find out the corresponding velocity distribution by employing Eq. (20). We continue this iteration step until convergence is attained on the solutions for E and $u(y)$.

The development of streaming potential on account of electrokinetic interactions can be seen as a parameter on how effectively one can harvest electrical energy from hydraulic energy. This is traditionally measured by the hydroelectric energy conversion efficiency η_s . The supplied mechanical energy to the flow through applied pressure gradient is transformed into the electrical energy by utilizing the streaming current and the streaming potential. Mathematically, the conversion efficiency can be expressed as [4,6]

$$\eta_s = \frac{I_s |E_s|}{\left| \frac{dp}{dx} \right| Q}. \tag{24}$$

In Eq. (24), I_s is the streaming current, E_s is the streaming potential field, and Q is the volumetric flow rate.

F. Expressions for volumetric flow rate and stress distribution

We obtain an analytical expression for the dimensionless volumetric flow rate Q_f . The general mathematical description of Q_f can be written as

$$Q_f = \frac{Q}{2aWU_{\text{ref}}} = \int_0^1 u(y) dy, \tag{25}$$

where the dimensional volumetric flow rate $Q = W \int_{-a}^a U dY$.

We perform the integration of Eq. (25) after substituting the analytical expression of $u(y)$ from Eq. (20), to yield the analytical expression

$$\begin{aligned} Q_f = & \frac{72\epsilon_s \text{Wi}_k^2 E}{\zeta \kappa^5} \left[\text{Li}_4(p) - \text{Li}_4(-p) + \frac{2}{3} \text{Li}_4(-e^{-\kappa} p) + \frac{1}{3} \text{Li}_4(-e^{\kappa} p) - \text{Li}_4(e^{-\kappa} p) \right] + \frac{72\epsilon_s \text{Wi}_k^2 E}{\zeta \kappa^4} [\text{Li}_3(-p) - \text{Li}_3(p)] \\ & + \frac{72\epsilon_s \text{Wi}_k^2 E^2}{\zeta^2 \kappa^3} \left[\text{Li}_2(p^2) - \frac{1}{3} \text{Li}_2(e^{-2\kappa} p^2) + \frac{\zeta}{36\epsilon_s \text{Wi}_k^2 E} \text{Li}_2(-p) \left\{ 2\epsilon_s \text{Wi}_k^2 \left(\frac{2\kappa^2 E^2}{\zeta^2} - 9 \right) - \kappa^2 \right\} \right. \\ & + \left. \frac{\zeta}{36\epsilon_s \text{Wi}_k^2 E} \text{Li}_2(p) \left(-\frac{4\epsilon_s \text{Wi}_k^2 \kappa^2 E^2}{\zeta^2} + 18\epsilon_s \text{Wi}_k^2 + \kappa^2 \right) \right] + \frac{24\epsilon_s \text{Wi}_k^2 E^2}{\zeta^2 \kappa^2} \left[\ln \left\{ \frac{(1-p^2)^3}{(e^{2\kappa} - p^2)} \right\} - \frac{\zeta}{2E} \ln \frac{1+p}{1-p} \right. \\ & + \left. \frac{2\kappa}{1-p^2} + \frac{\zeta^2}{60E^2} \right] + \frac{16\epsilon_s \text{Wi}_k^2 E^3}{\kappa \zeta^3} \left[\frac{p}{1-p^2} - \frac{pe^{\kappa}}{e^{2\kappa} - p^2} + \frac{1}{2} \text{Li}_2(pe^{-\kappa}) - \frac{1}{2} \text{Li}_2(-pe^{-\kappa}) - \frac{\kappa p(1+p^2)}{(1-p^2)^2} - \frac{\kappa}{2} \ln \frac{1-p}{1+p} \right] \\ & + \frac{2E}{\zeta \kappa} [\text{Li}_2(-pe^{-\kappa}) - \text{Li}_2(pe^{-\kappa})] + \frac{2E}{\zeta} \ln \frac{1-p}{1+p} + \frac{1}{3}. \end{aligned} \tag{26}$$

Similarly under Debye–Hückel linearization approximation, we substitute the analytical expression for velocity distribution from Eq. (21) into Eq. (25) and upon integration to obtain the corresponding closed form expression for Q_f as follows:

$$\begin{aligned} Q_f = & \frac{1}{20\kappa^4 \cosh^2(\kappa)} [\epsilon_s \text{Wi}_k^2 \{ 10\kappa^4 E^2 (3E - 2) - 3\kappa^2 (5E^2 + 30E - 2) - 540E \} + 5\kappa^4 (1 - 3E)] \\ & - \frac{\cosh(3\kappa)}{60\kappa^4 \cosh^3(\kappa)} [\epsilon_s \text{Wi}_k^2 \{ 10\kappa^4 E^3 + \kappa^2 (45E^2 + 90E - 6) + 540E \} + 5\kappa^4 (3E - 1)] \\ & + \frac{E \sinh(\kappa)}{36\kappa^5 \cosh^3(\kappa)} [\epsilon_s \text{Wi}_k^2 \{ 2\kappa^4 E (27 - 26E) + 27\kappa^2 (E + 12) + 648 \}] \\ & + [\epsilon_s \text{Wi}_k^2 \{ 2\kappa^4 E (2E + 27) + 27\kappa^2 (E + 12) + 648 \} + 18\kappa^4] \cosh(2\kappa) + 18\kappa^4. \end{aligned} \tag{27}$$

In order to obtain the expression for polymeric stress distribution, we begin by writing the pertinent relationships between shear (τ_{XY}) and normal (τ_{XX}) stresses. From simple manipulations between Eqs. (12)–(14), we can write this interrelationship as

$$\tau_{XY}^2 = \frac{\eta}{2\lambda} \tau_{XX}. \tag{28}$$

We now substitute Eq. (17) into Eq. (28) and to obtain the following expression for dimensionless normal stress τ_{xx} of the form

$$\tau_{xx} = \frac{\tau_{XX}}{\eta U_{ref} \bar{\kappa}} = 2 \frac{Wi_k}{\kappa^2} \left[\frac{E}{\zeta} \left(\frac{d\psi}{dy} \right) - y \right]^2. \tag{29}$$

We, may, perhaps, obtain the following equations for shear and normal stress components in dimensionless form [25,31]:

$$\tau_{xy} = y - \frac{4E\kappa p e^{\kappa(y-1)}}{\zeta \{1 - p^2 e^{2\kappa(y-1)}\}}, \tag{30a}$$

$$\tau_{xx} = 2 \frac{Wi_k}{\kappa^2} \left[y - \frac{4E\kappa p e^{\kappa(y-1)}}{\zeta \{1 - p^2 e^{2\kappa(y-1)}\}} \right]^2. \tag{30b}$$

Then again, the nondimensional equation for shear rate can be written as

$$\bar{\Upsilon} = \frac{\bar{\chi}}{(-U_{ref}/a)} = \left[y - \frac{4E\kappa p e^{\kappa(y-1)}}{\zeta \{1 - p^2 e^{2\kappa(y-1)}\}} \right] \times \left[1 + \frac{2\varepsilon_s Wi_k^2}{\kappa^2} \left\{ y - \frac{4E\kappa p e^{\kappa(y-1)}}{\zeta \{1 - p^2 e^{2\kappa(y-1)}\}} \right\}^2 \right], \tag{31}$$

where $\bar{\chi}$ is the dimensional shear rate.

Finally, the dimensionless shear viscosity profile, $\mu_s = \tau_{xy}/\bar{\Upsilon}$, is given by

$$\mu_s = \left[1 + \frac{2\varepsilon_s Wi_k^2}{\kappa^2} \left\{ y - \frac{4E\kappa p e^{\kappa(y-1)}}{\zeta \{1 - p^2 e^{2\kappa(y-1)}\}} \right\}^2 \right]^{-1}. \tag{32}$$

An obvious thing that can be noted from Eq. (32) is that one may calculate the dimensionless transverse averaged shear viscosity μ_{av} , defined as

$$\mu_{av} = \int_0^1 \mu_s dy. \tag{33}$$

We further note that for the Newtonian fluid, $\varepsilon_s Wi_k^2 = 0$, and thereby set the maximum limit for viscosity, $\mu_s = \mu_{av} = 1$.

III. RESULTS AND DISCUSSIONS

In the preceding section, we have derived analytical expressions for velocity profile, streaming potential, and flow rate for the transporting PTT fluid under the combined influences of pressure gradient and electrokinetics over low to large surface potentials. In this section, we shall try to shed light on the resulting hydrodynamics for the aforementioned situations. Now, before going into the detailed analysis, we first attempt to validate the present analytical formulation with the comparable data available in the literature. Accordingly, in Fig. 2(a), we plot the dimensionless velocity distributions across the channel width for the condition of $\varepsilon_s Wi_k^2 = 1$, $\kappa = 20$, and compare it between the current analytical solution with the analytical results reported by Afonso *et al.* [25]. Note that while validating the present model, we have obtained in Eq. (29) an analytical solution for the velocity distribution as given

in the literature by imitating the physical considerations used in Afonso *et al.* [25]. Furthermore, for streaming potential mediated pressure driven flows in a microchannel, we validate our analytic solutions as given by Eqs. (20) and (21) with the previously reported analytical result of the limiting linear case, $\varepsilon_s Wi_k^2 \rightarrow 0$. Therefore, as a limiting case of our analytical solution, the dimensionless velocity distribution across the microchannel cross section pertaining to Eq. (20) can be analytically expressed in the following form: $u(y) = \frac{4E}{\zeta} [\tanh^{-1}\{pe^{\kappa(y-1)}\} - \tanh^{-1}(p)] + \frac{1}{2}(1 - y^2)$. On the other hand, the corresponding analytic expression for Eq. (21) is obtained as $u(y) = \frac{1}{8\cosh^3(\kappa)} [\cosh\{\kappa(y+2)\} + 2E \cosh\{\kappa(y-2)\} - (2E + y^2 - 1)\{\cosh(3\kappa) + 3 \cosh(\kappa)\} + 2 \cosh(\kappa y)]$. We have verified these nondimensional velocity distributions with the previously published data by Yang and Kwok [66]. The comparison results are shown in Fig. 2(b) for $\kappa = 10$, $\zeta = 1$, and $Du = 0$, which matches closely with those of Yang and Kwok [66]. The agreement between the results obtained by the present analytical formalism and that of the literature in Fig. 2 serves as a testament towards the accuracy of the analytical method invoked in this research. In this context, it may be important to discuss the range of physical parameter spaces for generating numerical results. Towards this, we assume a typical non-Newtonian biofluid sample (take blood) at a reference temperature $T = 300$ K [5,23,67,68], for which $\rho \sim 10^3$ kg/m³, $\eta \sim 10^{-3} - 10^{-2}$ Pa s, $a \sim 10^{-4}$ m, and $\varepsilon \sim 702.24 \times 10^{-12}$ C²/Jm. For a $z : z$ symmetric electrolyte, the electrochemical constants may be taken as [67] $f \approx 10^{-12}$ N s/m, $\sigma_B \approx 10$ nS/cm. Furthermore, with a bulk ionic concentration (n_0) ranging from millimolarity to molarity [68], the range of dimensional zeta potential may vary in the tune of $\sim 10 - 50$ mV, whereas, the typical Stern layer conductivity value varies in the range $0 - 72$ nS/cm [5,68], and the dimensionless conductivity parameter may

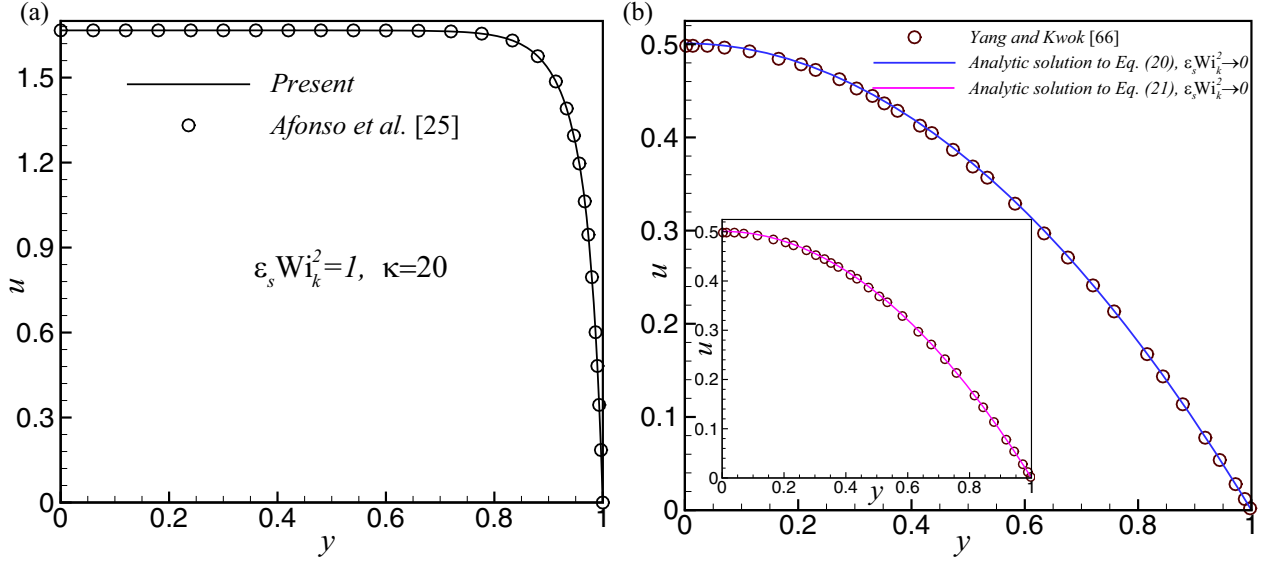


FIG. 2. (a) Dimensionless velocity distributions across the channel width at $\varepsilon_s Wi_k^2 = 1$, $\kappa = 20$. A comparison on the velocity data has been made between the current analytical solution and the analytical results reported by Afonso *et al.* [25]. (b) Nondimensional velocity profiles with y for $\kappa = 10$, $\zeta = 1$, $Du = 0$, and $\varepsilon_s Wi_k^2 \rightarrow 0$. The solid lines demonstrate the results from our analytical solution, whereas the markers represent the published data by Yang and Kwok [66].

take the value of $|\alpha| \sim 10$. We note that the width and longitudinal length of the channel usually ranges in the order of $W \sim L \sim O(10^3 \mu\text{m})$, whereas the half height of the channel is $a \sim O(10 \mu\text{m})$ [67,69]. Therefore, the corresponding dimensionless parameters may fall within the following range of parametric spaces: $\kappa \sim 10\text{--}40$, $\zeta \sim 1\text{--}10$, $\varepsilon_s Wi_k^2 \sim 0\text{--}2$, and the Dukhin number varying from 0 to 25. In the subsequent discussions, we highlight the implications of variations in these parameters on the overall electrohydrodynamic characteristics of PTT fluid in the microchannel.

A. Development of streaming potential and velocity distribution

We start by presenting the nature of the streaming potential development with Fig. 3(a), where we plot the magnitude of nondimensional streaming potential field (E) as a function of the dimensionless zeta potential (ζ) for different values of κ (the other pertinent parameters have been indicated in the caption). The general course of the figure [Fig. 3(a)] is that as the zeta potential is increased, the induced streaming potential field develops in such a way that the overall distribution obeys a bell-shaped curve followed by an asymptotic drift at the higher values of ζ [56]. This trend of variation can be explained by the fact that the degree of surface charging is continuously enhanced by increasing ζ . This, in turn, enhances the mobile counterion concentration in the EDL region therefore triggering the development of forward streaming current towards pressure gradient driven flow. On the other hand, the magnitude of the streaming potential is augmented owing to the increasing strength of the flow opposing back electrokinetic motion. The conflicting analogy of these two contrasting mechanisms leads to an instantaneous value of ζ for which the streaming potential field attains its peak value. Nevertheless, away from this threshold vicinity of ζ ,

predominant strength of the forward streaming current causes continuous reduction in the induced streaming potential in order to maintain the electroneutrality constraint. Moreover, in the diffuse zone of EDL, the effective pre-exponentiation factor is higher at the larger values of ζ thereby yielding a rapid decrement in the streaming potential magnitude [56]. It is definitely worth mentioning here that at each cross section of the microchannel, the nonlinear coupling between electrokinetic effects and non-Newtonian fluid rheology at the higher zeta potential regime cannot be superimposed for maintaining a consistent description of the electroneutrality. We further observe that as the dimensionless parameter κ increases, the streaming potential field has a decreasing trend and the lowest value corresponds to the situation at $\kappa = 40$. This is attributed to the fact that higher values of κ indicates thinner EDL, in which the Debye length is significantly lower than the characteristics dimension of the channel. The resulting consequence increases the ionic resistance thereby reducing the bulk ionic conductivity of the flow. At the situation of reduced bulk ionic conductivity, to balance the equivalent streaming current, a lower magnitude of streaming electric field may be induced in order to have a subsequent conduction current to satisfy electroneutrality constraint. The overall effect culminates in a feeble induced streaming potential field.

Figure 3(b) depicts the variation of the magnitude of dimensionless streaming potential E with the dimensionless viscoelastic set $\varepsilon_s Wi_k^2$ for different κ , while the other relevant parameters have been indicated in the caption. As evident from this figure and also seen from the inset, each $E - \varepsilon_s Wi_k^2$ curve is a straight line passing through the origin at $\varepsilon_s Wi_k^2 = 0$, indicating that starting from the Newtonian regime E increases linearly with $\varepsilon_s Wi_k^2$. This can be explained by the fact that increasing $\varepsilon_s Wi_k^2$, pointing to a deviation from the Newtonian behavior, causes a concurrent amplification in the bulk fluid velocity (as will be shown shortly, also, $Wi_k = \lambda \bar{\kappa} U_{\text{ref}}$).

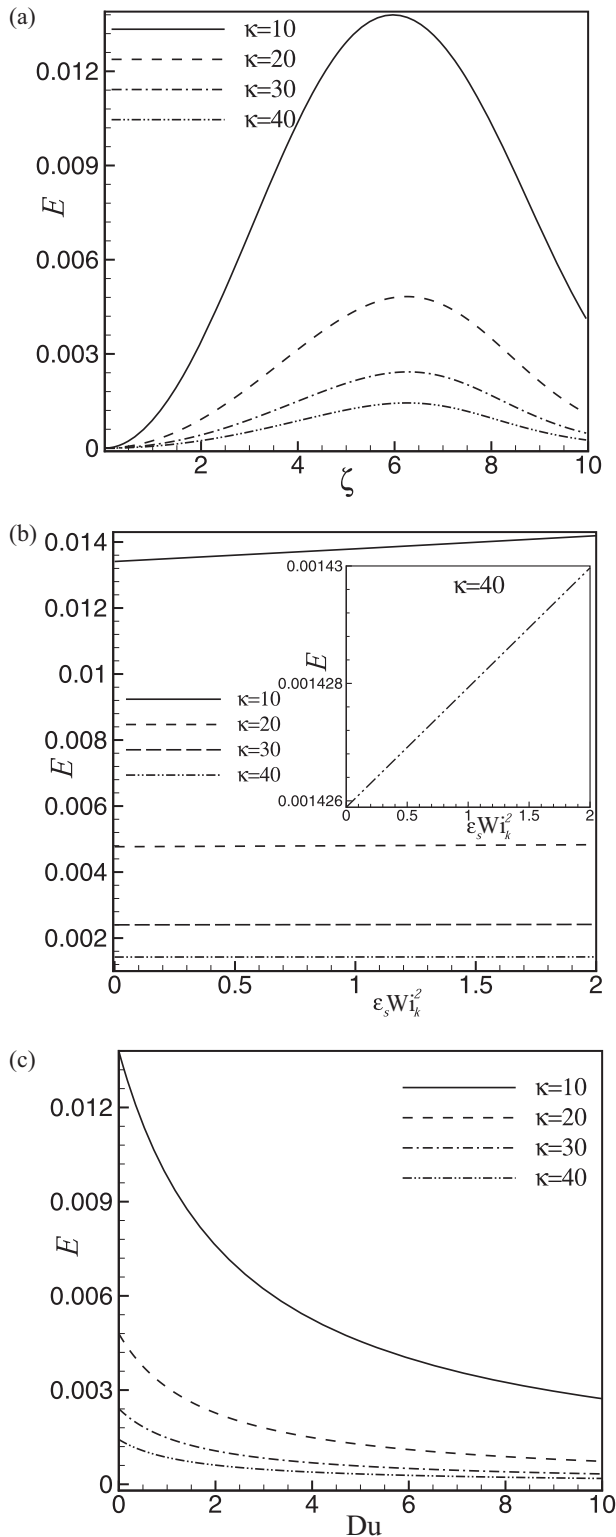


FIG. 3. Variation of the dimensionless induced streaming potential (E) with (a) dimensionless zeta potential for $Du = 0$, $\epsilon_s Wi_k^2 = 1$; (b) $\epsilon_s Wi_k^2$ for $\zeta = 6$, $Du = 0$; (c) Du for $\zeta = 6$, $\epsilon_s Wi_k^2 = 1$, at different values of κ .

An increase in bulk fluid velocity triggers the advective motions of mobile ions within the EDL. This, in turn, generates the larger ion flux in the EDL region thus resulting in the

generation of additional streaming current. The overall effect finally culminates in augmenting the streaming potential magnitude. Using the least square curve fit for (E , $\epsilon_s Wi_k^2$) data, the streaming potential at $\kappa = 10$ and 40 may be expressed by the following empirical relationships: $E_{\kappa=10} = 4 \times 10^{-4} \epsilon_s Wi_k^2 + 0.0134$, $E_{\kappa=40} = 10^{-6} \epsilon_s Wi_k^2 + 0.0014$, with R -squared (R^2) values of $R^2_{\kappa=10} = 0.98$ and $R^2_{\kappa=40} = 0.99$, respectively. Nevertheless, irrespective of the fluid rheological characteristics, the parameter κ primarily emerges as the deciding factor to mitigate the streaming potential magnitude.

To describe the impact of the stern layer conductivity on the streaming potential magnitude, in Fig. 3(c), we plot the variation of E as a function of Du for different values κ ; other relevant dimensionless parameters are mentioned in the caption. It can be found from Fig. 3(c) that as the value of Du increases, all the curves portray a decreasing trend in E . Intuitively, an increase in the Dukhin number leads to the increase in Stern layer conductivity. As a consequence of this, the component of conduction current through the Stern layer also increases that along the bulk liquid. Larger Stern layer conductivity leads to the formation of an alternate less-resistive path for the conduction current to flow [46]. Therefore, ignoring the contribution of the conduction current through the bulk fluid, the streaming current equilibrates with the corresponding conduction current through the Stern layer. This implies that a lower magnitude of the electric potential is sufficient enough to stabilize the streaming current for satisfying the electroneutrality. This in turn leads to a lower magnitude of the induced streaming potential field. An obvious thing to note from Fig. 3(c) is that a larger value of κ leads to a lower magnitude of E . The explanation behind such a trend has already been briefed in Fig. 3(a).

In Fig. 4(a) we plot the dimensionless velocity profiles for different values of nondimensional surface zeta potential ζ (other pertinent parameters have been given in the caption). It may be noted that owing to the combined consequences of applied pressure gradient and induced electrokinetic forcing, the velocity profile exhibits a parabolic distribution. A general trend in this plot is that when the effects of surface charging is considered, increasing the degree of ζ results in corresponding amplifications in the velocity magnitude in the microchannel. Interestingly, this augmentation in velocity distribution is palpable at the lower to moderate regimes of wall zeta potential, namely, in the range of $1 \leq \zeta \leq 6$. In contrast, for higher values of zeta potentials ($\zeta > 6$), further increase in ζ causes a gradual reduction in the velocity magnitude. This trend of velocity distribution can be explained as follows. As ζ increases, concentration of the ions in the EDL becomes more and causes an enhancement in the advective transport of the bulk fluid. This leads to a higher amplification of the flow velocity. On the other hand, as the advective strength of the ionic species increases, the back electrokinetic strength becomes more. The consequential influence is perceived by increasing the effective electroviscous retardation thus causing a gradual drop in the flow velocity. The competing mechanisms of these two contrasting influences lead to a threshold magnitude of $\zeta \sim 6$ after which velocity profiles show its steady decrement. It is worth mentioning here that the peak point of both velocity and streaming potential curves share a common magnitude of surface charging at $\zeta \sim 6$ [see Fig. 3(a)].

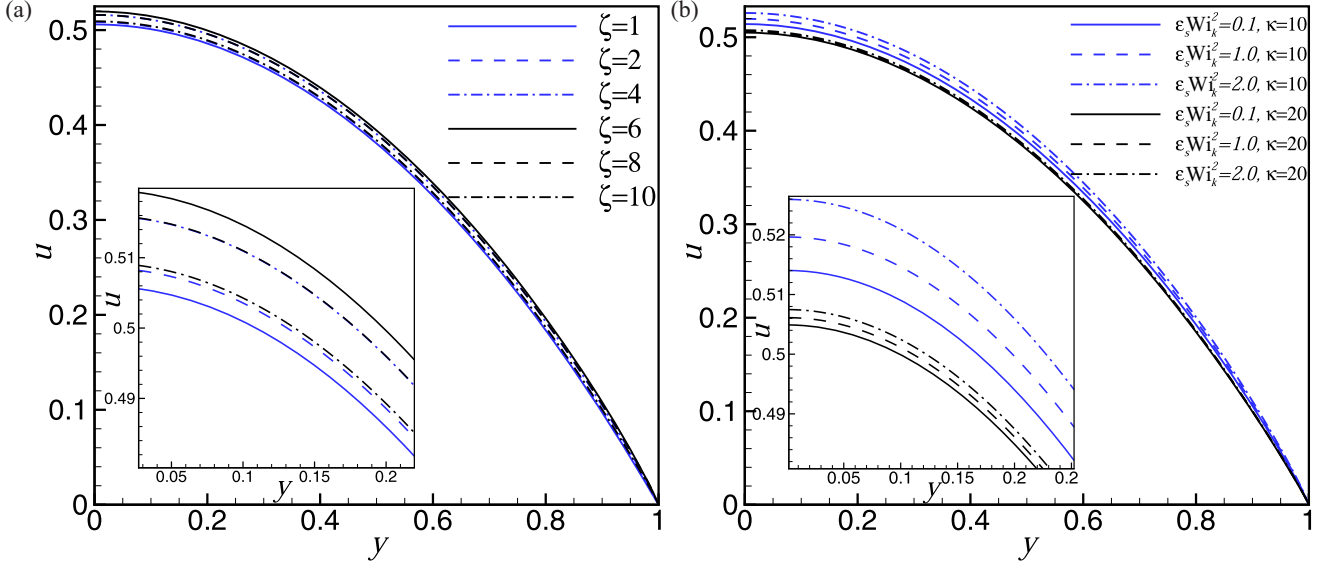


FIG. 4. Variation of the dimensionless velocity (u) along the cross section of the confinement (y) for (a) different ζ at $Du = 0$, $\kappa = 10$, $\varepsilon_s Wi_k^2 = 1$; (b) different $\varepsilon_s Wi_k^2$ at $\zeta = 6$, $Du = 0$, $\kappa = 10$.

We next analyze the influences of the dimensionless viscoelastic set $\varepsilon_s Wi_k^2$ on the nondimensional velocity distribution. Towards this, in Fig. 4(b), the variation of nondimensional velocity (u) along the cross section of the confinement has been plotted as a function of y for various values of $\varepsilon_s Wi_k^2$ and κ , while in the caption other relevant parameters have been referred to. From Fig. 4(b), it is seen that there is an augmentation of the velocity distribution as the dimensionless parameter $\varepsilon_s Wi_k^2$ increases. The same behavior is noticed both at $\kappa = 10$ and $\kappa = 20$, respectively. Irrespective of the values of κ , it is observed that velocity gradients within the EDL increase for larger magnitudes of $\varepsilon_s Wi_k^2$. Increase in the fluid velocity with increasing $\varepsilon_s Wi_k^2$ is attributed to an amplified shear thinning characteristic of the fluid [70]. We further observe that although the overall velocity distribution is parabolic, in the channel centerline the velocity profiles flatten with increasing values of $\varepsilon_s Wi_k^2$. Similar behavior is also noticed for non-Newtonian power-law fluids obeying pseudoplastic rheology. In addition, again it can be seen that velocity loses its strength when the dimensionless parameter κ is enhanced. This is due to the fact that an increase in κ demonstrates a corresponding reduction in E (see Fig. 3), which results in the shear rate ($\bar{\gamma}$) to decrease synchronously, since $\bar{\gamma} \propto E^3$ [see Eq. (31)]. As a consequence, there is a considerable enhancement in the shear viscosity (μ_s), since $\mu_s \propto 1/\bar{\gamma}$ [see Eq. (32)]. Accordingly, the effective resistance to the flow increases, culminating in lower magnitudes of fluid velocities with higher values of κ .

B. Electrohydrodynamic characteristics

In this section, to analyze the electrohydrodynamic characteristics, we begin by characterizing the consequences of physicochemical condition and fluid rheology on the dimensionless volumetric flow rate Q_f . In Fig. 5(a) we depict the variation of Q_f as a function of ζ for different values of κ ; the other chosen parameters have been given in the caption. It

can be seen that as the magnitude of surface charging ζ is increased, there is an exponential growth in Q_f before reaching its maxima at $\zeta \sim 6$ followed by an asymptotic decrease in Q_f for further augmenting the values of ζ . These two contrary paradigms of the hydrodynamic scenario at different values of ζ are attributed to the corresponding corroboration with the streaming potential development, which also follows an analogous trend [see Fig. 3(a)]. It has already been discussed in Fig. 4(a) that gradual development in flow velocities up to a typical threshold value of dimensionless zeta potential ($\zeta \leq 6$) leads to an equivalent behavior in volumetric flow rates. In contrast, the regime beyond $\zeta > 6$ results in a corresponding decrement in flow velocities and therefore ensuing reduction in the dimensionless volumetric flow rate magnitude Q_f . We see that as the parameter κ is increased, there is a steady drop in the volumetric flow rate.

Figure 5(b) displays the variation of Q_f with $\varepsilon_s Wi_k^2$ for varying magnitudes of κ (other relevant parameters are given in the caption). It is found that as the value of $\varepsilon_s Wi_k^2$ increases, all the curves of dimensionless volumetric flow rates follow a linear growth. The dependence of Q_f on $\varepsilon_s Wi_k^2$ at $\kappa = 10$ and 40 can be approximated by the following empirical relationships: $[Q_f]_{\kappa=10} = 5.2 \times 10^{-3} \varepsilon_s Wi_k^2 + 0.3458$, $[Q_f]_{\kappa=40} = 0.3 \times 10^{-3} \varepsilon_s Wi_k^2 + 0.3347$. The corresponding R^2 values for these correlations are $R_{\kappa=10}^2 = 0.99$ and $R_{\kappa=40}^2 = 0.98$. It has already been briefly presented in the preceding section that increasing the nondimensional viscoelastic set $\varepsilon_s Wi_k^2$ brings about a shear thinning effect in the flow rheology. This, in effect, augments the fluid velocity within the microchannel thereby leading to a gradual enhancement in the flow rate. Another point to observe from Fig. 5(b) is that for higher values of κ , the gradient of the volumetric flow rate curve $[\partial Q_f / \partial (\varepsilon_s Wi_k^2)]$ becomes smaller and the least value is attained at $\kappa = 40$. In an effort to obtain a relationship between the maximum and minimum gradients, we employ the empirical relationships of Q_f to yield $[\partial Q_f / \partial (\varepsilon_s Wi_k^2)]_{\kappa=10} = 17.33 [\partial Q_f / \partial (\varepsilon_s Wi_k^2)]_{\kappa=40}$.

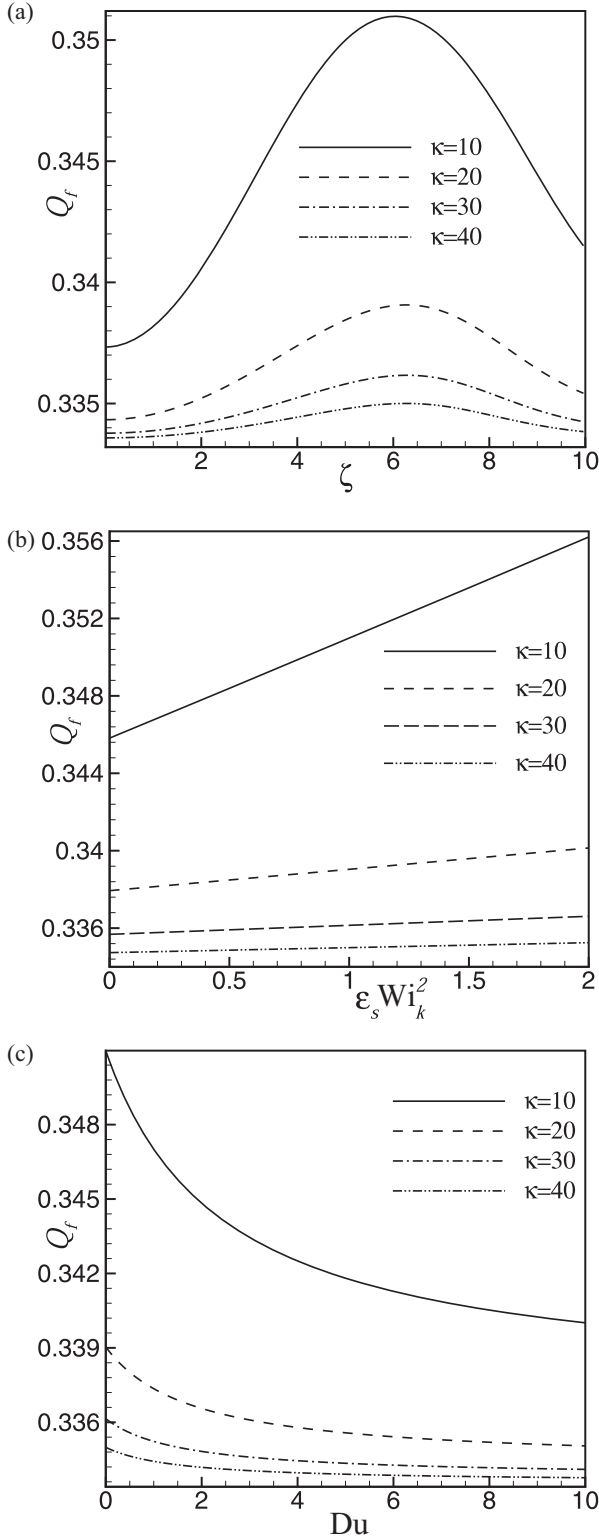


FIG. 5. Variation of the dimensionless volumetric flow rate (Q_f) with (a) dimensionless zeta potential for $Du = 0$, $\varepsilon_s Wi_k^2 = 1$; (b) $\varepsilon_s Wi_k^2$ for $\zeta = 6$, $Du = 0$; (c) Du for $\zeta = 6$, $\varepsilon_s Wi_k^2 = 1$, at different values of κ .

In Fig. 5(c), we portray the distribution of Q_f as a function of stern layer conductivity Du . The other selected parameter values are given in the caption. From the figure, it can

be seen that as Du is increased, the volumetric flow rate follows a similar trend to that obtained for the Fig. 3(c). Such a trend of decrement in flow rates with increasing Stern layer conductivity can again be explained on similar lines of reduction in the induced streaming potential E with a consequent increase in Du . As already mentioned briefly, in the perspective of Fig. 3(c) the Stern layer conductivity plays an opposing role for the establishment of E . Therefore, the contribution of the electrokinetic inertia force to the bulk flow field reduces for increasing Du . Eventually, the flow velocity decreases; this in turn leads to decay in the volumetric flow rates. It is seen that the magnitude of reduction in Q_f over the ranges of κ is maximum at $\kappa = 10$, whereas the slope of the curve $\partial Q_f / \partial (Du)$ decreases with augmenting values of the parameter κ .

In Figs. 6(a) and 6(b), we show the variation of the dimensionless normal stress, τ_{xx} [Fig. 6(a)], and shear stress, τ_{xy} [Fig. 6(b)], components across the microchannel (y) for different values of ζ , while the other appropriate parameters have been indicated in the caption. In general, it is observed from Fig. 6 that at the channel centerline, both of the stress components are closer to zero. Proceeding towards the channel wall, the stress components progressively increase and start to diverge from its linear trend at the transit point T . This follows a sudden jump in stress distribution nearer the vicinity of the confining walls. The characteristic of stress distribution is a result of the alternation in velocity gradients in a more dominant fashion owing to the combined presence of the interfacial electrokinetic forcing and the applied pressure gradient inside the EDL region [31,71]. On the other hand, to balance the mass conservation within the flow domain, towards the core of the channel, there will be a corresponding decrement in the velocity gradient for increasing ζ . This, in turn, brings about an emergence of the transit point T on the τ - y curve, as shown in Figs. 6(a) and 6(b). The overall consequences culminate in reducing the stress components until $\tau_{xx}, \tau_{xy} \rightarrow 0$ at the channel core. We see from panels (a) and (b) that both τ_{xx} and τ_{xy} increase as the surface zeta potential increases. Interestingly, we observe from the insets that even though τ_{xx}, τ_{xy} increases with increasing ζ , beyond a threshold magnitude of $\zeta > 6$, there is a steady drop in both the normal and shear stress components. Therefore, for higher zeta potentials, the magnitudes of τ_{xx}, τ_{xy} are lower than that of the case with lower ζ , which is exactly the same trend as predicted for other situations noted previously. It is worth mentioning here that the development of induced streaming potential field for increasing the degree of surface charging primarily dominates all of the associated electrohydrodynamic phenomena inside the microchannel. Therefore, the stress components are no exceptions, since from Eqs. (30a) and (30b) one may write $\tau_{xx} \propto E^2$ and $\tau_{xy} \propto E$. Thus, τ_{xx}, τ_{xy} are also implicitly adhering to the analogous trend on the development of the induced streaming potential field at the lower, moderate to higher zeta potential magnitudes [see Fig. 3(a)]. Comparing panels (a) and (b), it is seen that in the near wall region, there is an acute variation in the normal stress component when compared to that of the shear stress as because $\tau_{xx} \propto \tau_{xy}^2$ [refer Eq. (30)].

To analyze the impact of viscoelastic influence on the normal and shear stress components, in Figs. 7(a) and 7(b), we

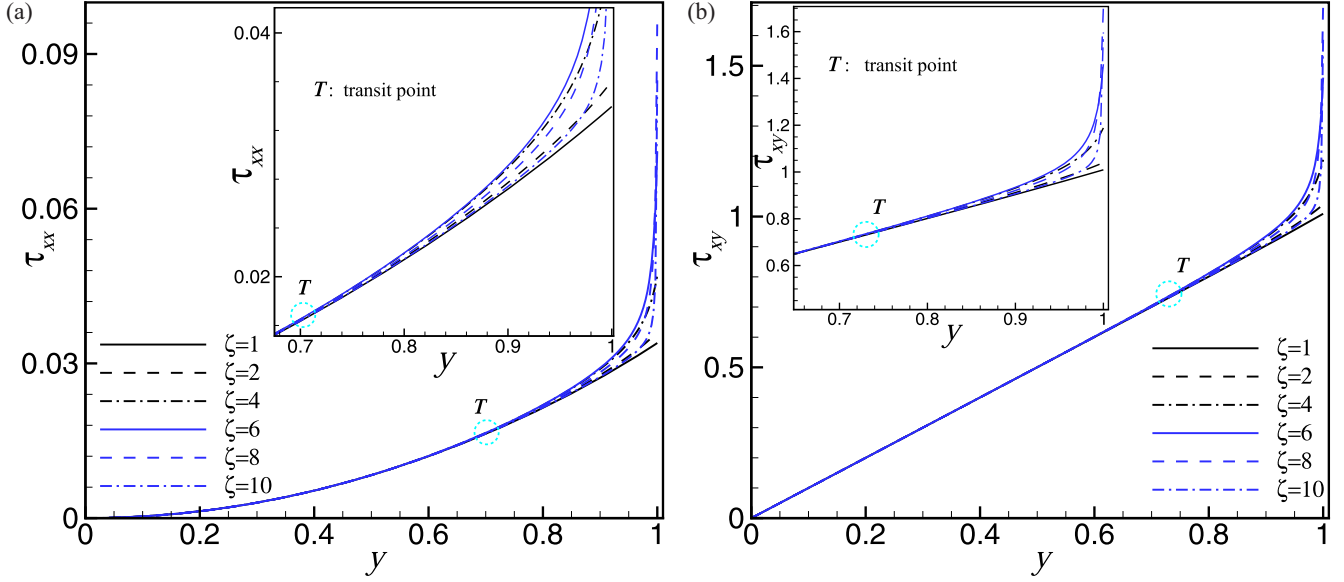


FIG. 6. Variation of the dimensionless (a) normal stress τ_{xx} and (b) shear stress τ_{xy} components across the microchannel (y) for different values of ζ at $Du = 0$, $\kappa = 10$, $\varepsilon_s Wi_k^2 = 1$.

depict the variation of τ_{xx} [Fig. 7(a)], and τ_{xy} [Fig. 7(b)], with y for different values of $\varepsilon_s Wi_k^2$ (the other pertinent parameters have been mentioned in the caption). It is apparent from these figures that increasing $\varepsilon_s Wi_k^2$ causes an enhancement in stress components. An enhancement in $\varepsilon_s Wi_k^2$ implies a paradigm shift in fluid rheology tending towards an intensified shear thinning regime. Thus, for higher values of $\varepsilon_s Wi_k^2$ there is a continuous gain in the flow velocity. This consequently leads to significant alternation in the velocity gradients, which, in effect, results in a concomitant augmentation in the stress components. An important aspect of the stress curve can be noticed that for Newtonian fluids at $\varepsilon_s Wi_k^2 = 0$, the normal stress component has zero value; in stark contrast, the shear

stress component has a nonzero linear variation with y . Moreover, the magnification of stress components with increasing $\varepsilon_s Wi_k^2$ is found to be more pronounced for τ_{xx} , whereas a very weak influence is witnessed on τ_{xy} . This can be explained from Eq. (30) where the τ_{xx} is found to be directly proportional to Wi_k , whereas τ_{xy} has an indirect relationship with Wi_k through the induced streaming potential field E , which is a function of $\varepsilon_s Wi_k^2$ [see Eq. (23)].

To investigate the effect of surface charging on the dimensionless shear viscosity μ_s , we plot the variation of the dimensionless shear viscosity across the microchannel (y) for different ζ in Fig. 8(a). In the caption, we have mentioned the other related parameters. Figure 8(a) shows that across

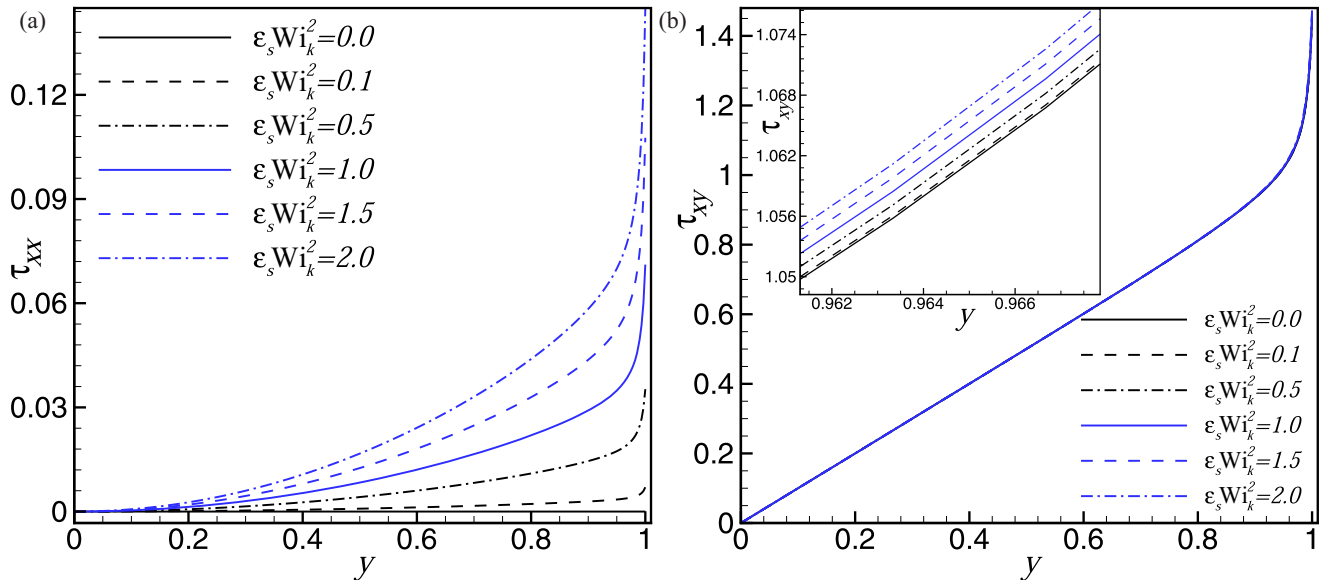


FIG. 7. Variation of the dimensionless (a) normal stress τ_{xx} and (b) shear stress τ_{xy} components across the microchannel (y) for different values of $\varepsilon_s Wi_k^2$ at $Du = 0$, $\kappa = 10$, $\zeta = 6$.

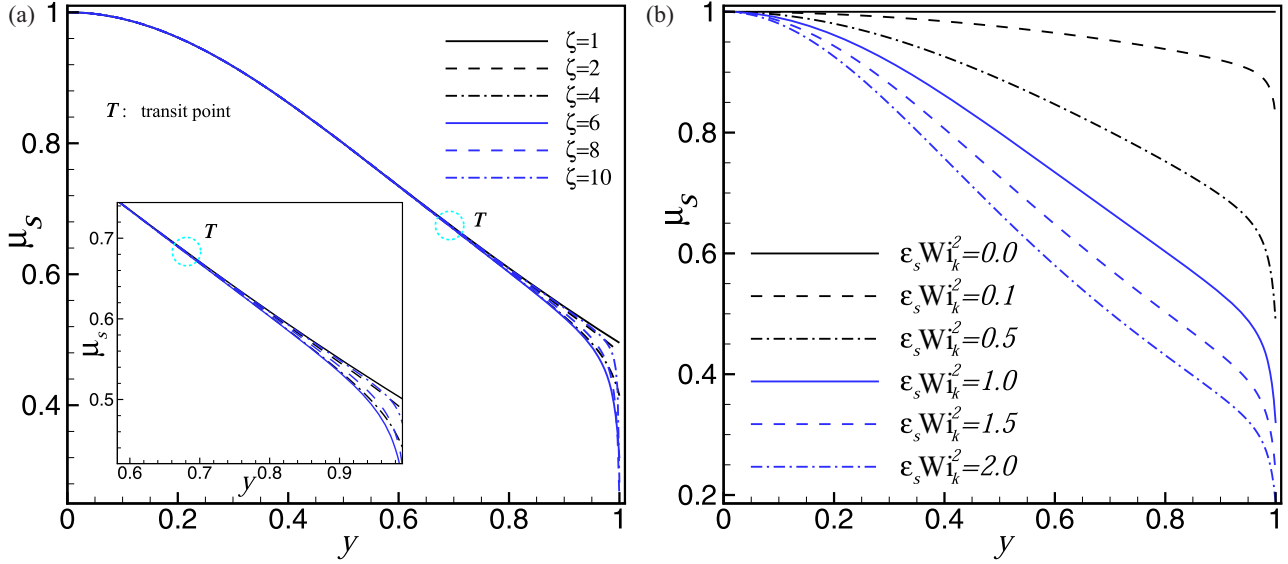


FIG. 8. Variation of the dimensionless shear viscosity (μ_s) along the cross section of the confinement (y) for (a) different ζ at $Du = 0$, $\kappa = 10$, $\varepsilon_s Wi_k^2 = 1$; (b) different $\varepsilon_s Wi_k^2$ at $\zeta = 6$, $Du = 0$, $\kappa = 10$.

the microchannel, μ_s progressively decays to its minimum value at the near wall region. We offer a physical explanation of this behavior as follows. At the core of the channel, the lower magnitude of the velocity gradient sets the viscosity value to a higher side, notably, at the centerline ($y = 0$); the dimensionless viscosity yields its peak magnitude of $\mu_s \approx 1$. In contrast, continuing enhancements in velocity gradients approaching towards the channel walls lead to a sharp drop in μ_s . Increasing the zeta potential significantly modulates the dimensionless shear viscosity at the near wall region thereby causing the $\mu_s - \zeta$ curve to bifurcate at the transit point T . This explains the fact that in the EDL region, increasing the magnitude of surface charging triggers the strength of the ionic advective transport, which, in turn, enhances the fluid velocity gradient and thereby proportionate alternation in the dimensionless viscosity. An important thing to note from this figure is that μ_s is lower for higher ζ , nevertheless, beyond a threshold value of $\zeta = 6$ (see inset), μ_s increases with increasing ζ . This is due to the fact that $\mu_s \propto 1/E^2$ [see Eq. (32)] thereby corroborating the functional dependence of E with ζ , as shown in Fig. 3(a).

We plot the variation of the μ_s with y in Fig. 8(b) for different $\varepsilon_s Wi_k^2$ (other constant parameter values have been mentioned in the caption). It emerges from this figure that increasing $\varepsilon_s Wi_k^2$ causes a striking drop in the dimensionless viscosity. This decrease in μ_s is attributed to the fact that a higher magnitude of $\varepsilon_s Wi_k^2$ severely augments the shear thinning characteristics of the PTT fluid, which causes an amplification in the flow velocity gradients. This adequately reduces the resistance to flow and thus lessens the shear viscosity. A point to mention from Fig. 8(b) is that the viscosity profile is spatially invariant for the Newtonian fluid at $\varepsilon_s Wi_k^2 = 0$ and yields a constant value of $\mu_s = 1$. A closer look into Fig. 8(b) tells that the viscosity curve does not follow a monotonic drop from the core of the channel, rather showing a sudden dip in the EDL region, nearer the channel wall. This is as attributable to the rapid changes in flow

velocity gradients primarily taking place in the near wall region.

Now, we examine the influence of various electrohydrodynamic parameters on the dimensionless transverse averaged shear viscosity μ_{av} . Towards this, in Figs. 9(a)–9(c), we show the functional dependence of μ_{av} with different electrohydrodynamic parameters ζ [in Fig. 9(a)], $\varepsilon_s Wi_k^2$ [in Fig. 9(b)], and Du [in Fig. 9(c)], respectively (in the caption, we have indicated the other representative parameter values). The results are shown for different κ values. Several appealing features are immediately evident from Fig. 9. It is seen from Fig. 9(a) that as the zeta potential increases, the averaged shear viscosity sharply drops to its minimum value around $\zeta \sim 6$; afterward, there is a steady growth of μ_{av} until it becomes asymptotically invariant for larger values of ζ . Intuitively, an enhancement in ζ leads to the reduction in μ_s thereby yielding a corresponding decrement in μ_{av} . On the other hand, beyond the point of minima at $\zeta \sim 6$, the shear viscosity increases therefore causing an equivalent increase in the average viscosity. Interestingly, the $\mu_{av} - \zeta$ curve is an inverted version of the $E - \zeta$ distribution [refer to Fig. 3(a)], because their mutual dependence follows an inverse relationship, $\mu_{av} \propto 1/E$ for constant ζ . The parameter κ has a noteworthy impact on augmenting the values of μ_{av} as portrayed in Fig. 9(a). Figure 9(b) shows that with an increase in $\varepsilon_s Wi_k^2$, there is an exponential decrease in the average shear viscosity. The physical explanation behind such a trend has already been discussed in Fig. 8(b). We have seen from Fig. 8(b) that there is a dramatic reduction in μ_s with increasing $\varepsilon_s Wi_k^2$; this essentially culminates in an overall drop of μ_{av} for higher values of $\varepsilon_s Wi_k^2$. A least square curve fit on $(\mu_{av}, \varepsilon_s Wi_k^2)$ data yields an empirical relationship for the prediction of μ_{av} as a function of $\varepsilon_s Wi_k^2$ at $\kappa = 10$ (with $R^2 = 0.97$): $\mu_{av} = -0.012(\varepsilon_s Wi_k^2)^3 + 0.0892(\varepsilon_s Wi_k^2)^2 - 0.2915(\varepsilon_s Wi_k^2) + 0.9922$. A very marginal variation in μ_{av} is seen for increasing κ ; nevertheless, from the insets it is found that the least value of μ_{av} is always at $\kappa = 10$. The effect of the Stern layer conductivity plays a

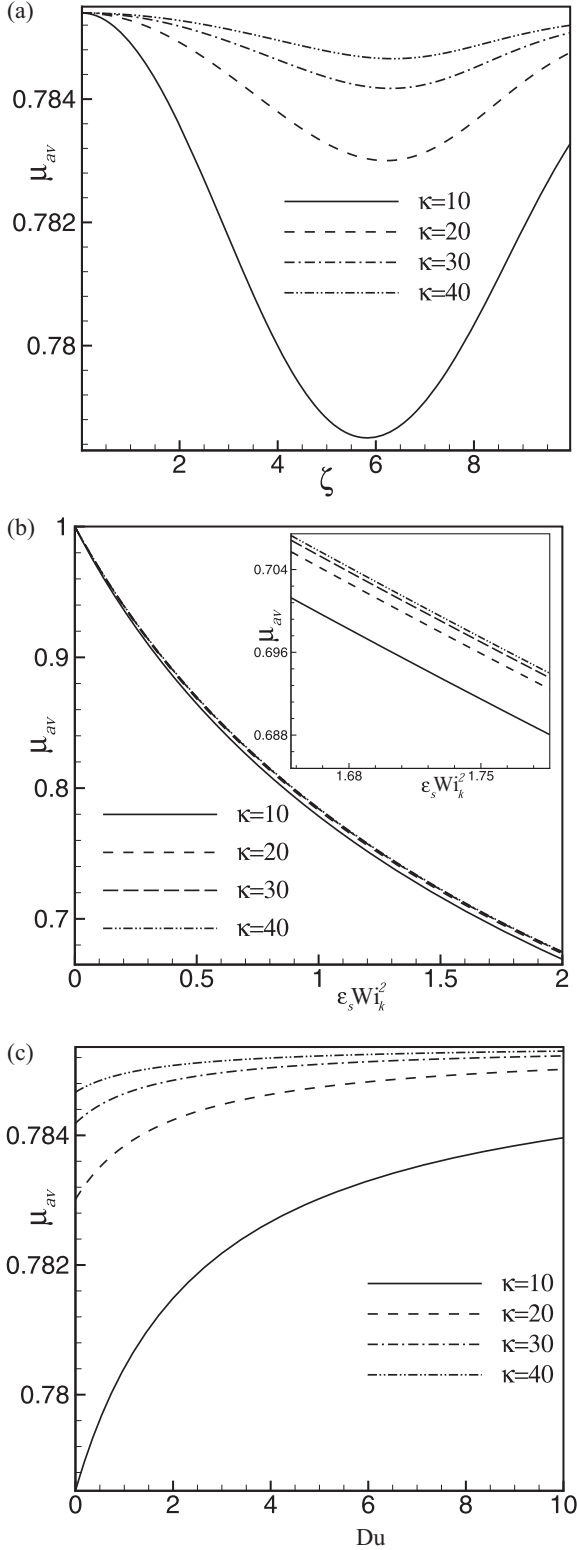


FIG. 9. Variation of the dimensionless transverse averaged shear viscosity (μ_{av}) with (a) dimensionless zeta potential for $Du = 0$, $\varepsilon_s Wi_k^2 = 1$; (b) $\varepsilon_s Wi_k^2$ for $\zeta = 6$, $Du = 0$; (c) Du for $\zeta = 6$, $\varepsilon_s Wi_k^2 = 1$, at different values of κ .

significant role in amplifying the average viscosity magnitude, as emerging from Fig. 9(c). It can be found that there is an exponential rise of μ_{av} with an increase in the Dukhin

number Du . As the Stern layer conductivity is increased, we note from Fig. 3(c) that there is a steady drop in the induced streaming potential field. This, in turn, brings about a lower flow velocity magnitude by exerting more resistance to the fluid motion, thus resulting in an intensification of μ_{av} values (also, $\mu_{av} \propto 1/E$). The inverse proportionality between μ_{av} and E yields the μ_{av} – Du curve shown in Fig. 9(c) to be an inverted description of E – Du distribution displayed in Fig. 3(c). Enhancement in κ yields a significant increase in μ_{av} . On the contrary, we notice that the slope of the μ_{av} – Du curve reduces with increasing values of the parameter κ .

C. Hydroelectrical energy conversion efficiency

Towards examining the influence of interfacial electrokinetics and viscoelasticity on the hydroelectrical energy conversion efficiency η_s , we first consider the situation in which the degree of surface charging is varied by means of low to high zeta potentials. We plot the variation of η_s in Fig. 10(a) as a function of the ζ , for illustrative values of $\kappa = 10, 20, 30$, and 40 , respectively. The other parameters are mentioned in the figure caption. It is evident from the figure that with increasing the values of ζ , a giant augmentation in the energy conversion efficiency may be achieved until the peak saturation limit in the neighborhood of $\zeta \sim 6$ is reached. This increase in conversion efficiency with increase in ζ is attributed to the concurrent enhancements in ionic advection and thereby rapid amplification in the induced streaming potential field. In contrast, for the remaining higher zeta potential regime, $6 < \zeta \leq 10$, the conversion efficiency drops with further increasing the values of ζ . This can again be explained by the fact that at large zeta potentials, $\zeta > 6$, the formation of a reverse streaming potential strengthens the back electrokinetic transport and therefore calls for a reduced streaming current for satisfying the electroneutrality. Furthermore, the conflux of conduction and streaming currents adjusts itself such that beyond a critical magnitude of ζ there is a gradual drop in the streaming potential field and thus a consequent decrement in the energy conversion efficiency. It may be mentioned here that the trend of variation of η_s – ζ curve is in line with that displayed in Fig. 3(a).

Figure 10(b) depicts the variation of η_s with $\varepsilon_s Wi_k^2$ for different values κ (other related parameters are mentioned in the caption). It is apparent from this figure and also from the inset that as the value of $\varepsilon_s Wi_k^2$ increases, the characteristic trend of the energy conversion efficiency displays a perfectly linear relationship. This suggests that deviating from the classical Newtonian paradigm at $\varepsilon_s Wi_k^2 = 0$, there is a continuous augmentation in the energy conversion efficiency. Again, an empirical equation of η_s as a function of $\varepsilon_s Wi_k^2$ via least square fit of the $(\eta_s, \varepsilon_s Wi_k^2)$ data at two representative values of $\kappa = 10, 40$, may be obtained as $[\eta_s]_{\kappa=10} = 6 \times 10^{-4} \varepsilon_s Wi_k^2 + 0.0128$, $[\eta_s]_{\kappa=40} = 2 \times 10^{-7} \varepsilon_s Wi_k^2 + 8 \times 10^{-5}$, where, $R_{\kappa=10}^2 = 0.98$ and $R_{\kappa=40}^2 = 0.99$, respectively. The physical reason behind this augmentation of η_s with increasing values of $\varepsilon_s Wi_k^2$ can be explained by looking into the nature of the variations in the induced streaming potential and velocity fields in Figs. 3(b) and 4(b), where we found that both of them increase profoundly with enhancing magnitudes of $\varepsilon_s Wi_k^2$. Thus increasing magnitudes of $\varepsilon_s Wi_k^2$ leads to increased energy conversion efficiency.

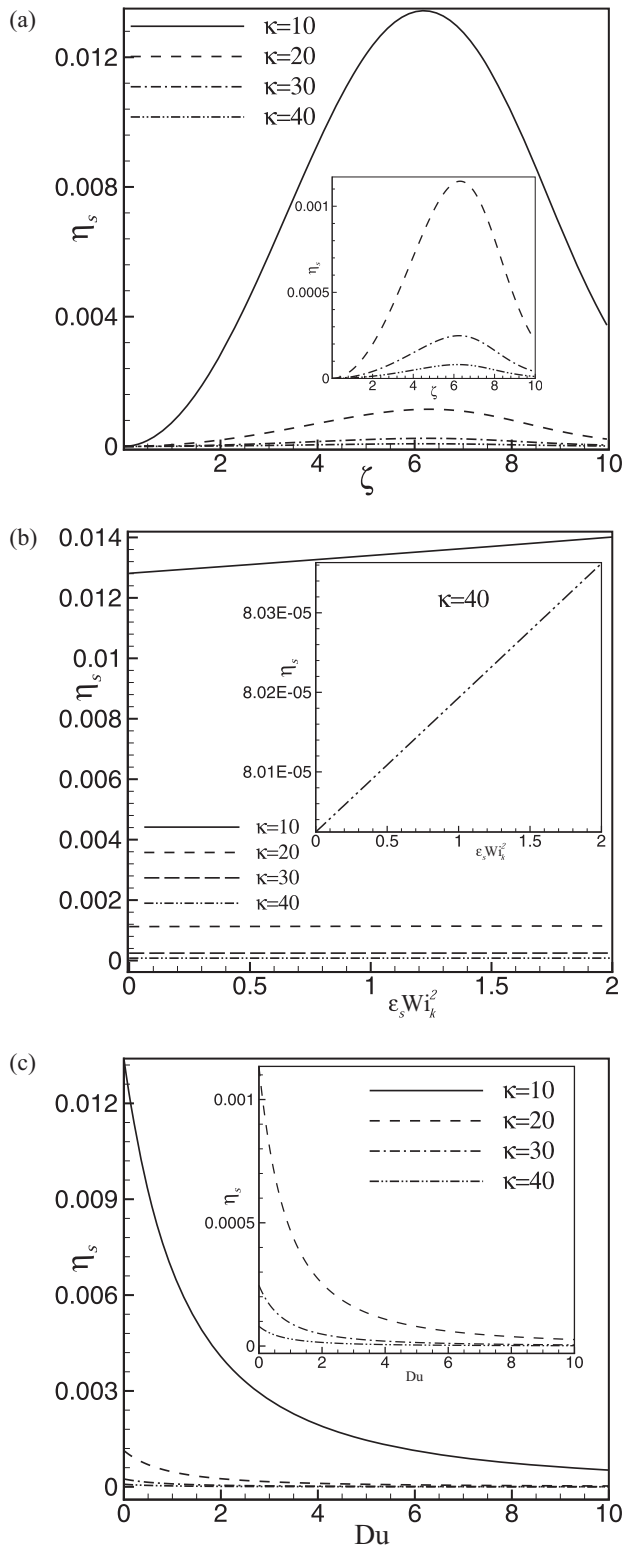


FIG. 10. Variation of the hydroelectrical energy conversion efficiency (η_s) with (a) dimensionless zeta potential for $Du = 0$, $\epsilon_s Wi_\kappa^2 = 1$; (b) $\epsilon_s Wi_\kappa^2$ for $\zeta = 6$, $Du = 0$; (c) Du for $\zeta = 6$, $\epsilon_s Wi_\kappa^2 = 1$, at different values of κ .

In an attempt to illustrate the implications of the Stern layer conductivity on the energy conversion efficiency, in Fig. 10(c), we depict the variation of η_s as a function of Du for various

values of κ . The supplementary pertinent parameters are given in the caption. Figure 10(c) reveals that the distribution of the energy conversion efficiency curve follows an exponential decay with increasing the Stern layer conductivity (Du). This is owing to the fact that there is an exponential drop in the induced streaming potential field with increasing the magnitudes of Du [see Fig. 3(c)]. As a consequence, a higher value of the Stern layer conductivity is always associated with a lower magnitude of the energy conversion efficiency. A general point to note from Fig. 10 is that an enhancement in the relative sizes of the microchannel, as guided by larger κ values, leads to a drastic reduction in the energy conversion efficiency. The physical reason behind such a trend is due to the fact that higher values of κ contribute in reducing the strength of the induced streaming potential field; this, in turn, results in lowering the magnitudes of η_s .

Towards highlighting the typical results on the combined electrohydrodynamic consequences, we finally show two representative cases of flow rate and energy conversion efficiency in Figs. 11(a) and 11(b). We plot Q_f [Fig. 11(a)] and η_s [Fig. 11(b)] as a function of ζ and $\epsilon_s Wi_\kappa^2$ for constant values of the parameters, $\kappa = 10$, $Du = 0$. This figure essentially corroborates the situations as portrayed in Figs. 5 and 10, respectively. A general inspection of Fig. 11 concedes that for specific combinations of ζ and $\epsilon_s Wi_\kappa^2$ one may achieve a maximization in flow rates and hydroelectric energy conversion efficiency. The optimal regime for the energy conversion efficiency, as recognized from the figure, falls within the narrow band of zeta potentials. Nevertheless, the corresponding regime for flow rates is always lying at a distinctive axial location of $\zeta \sim 6$, $\epsilon_s Wi_\kappa^2 \sim 2$, respectively. Therefore, from these plots, one may conclude that it is possible to modulate both hydroelectrical conversion efficiency and flow rates by the combined consequences of rheology and interfacial electrokinetics. This result may perhaps be useful for the microfluidic experiments and design of advanced smart sensors within the cognizance of electrohydrodynamics.

It is essential to mention that another phenomenon that takes place in this range of geometric scales is the formation of a polymer-depleted layer (PDL), because of the migration of polymer chains from the wall region to the centerline of the channel [62,72]. The mechanism that drives the flow does not affect the generation of this PDL and therefore it is inherent to both electrokinetic and pressure-driven flow of non-Newtonian fluid in a microchannel. This issue was explicitly addressed recently by Moschopoulos *et al.* [62]. They have performed a theoretical investigation on the electro-osmotic flow of polyethylene oxide (PEO) chains dissolved in a NaCl aquatic solvent in a microchannel. Their [62] study revealed that for the solution of 0.1% PEO, the theoretical results of the mean velocity on the applied electric field, taking into account the viscous contribution of the solvent in the solution phase, matches well with the experiments of Huang *et al.* [73]. In contrast, neglecting the viscous solvent causes overestimation in the mean velocity. Furthermore, the thickness of this PDL for the 0.1% PEO solution is 5 nm, and it is independent of the applied electrical field [62]. Perhaps it is also dependent on the elastic nature of the fluid. With an increase in PEO percentages, the increase in the PDL thickness is small for lower values of the imposed electric field (E_{xx}), whereas for

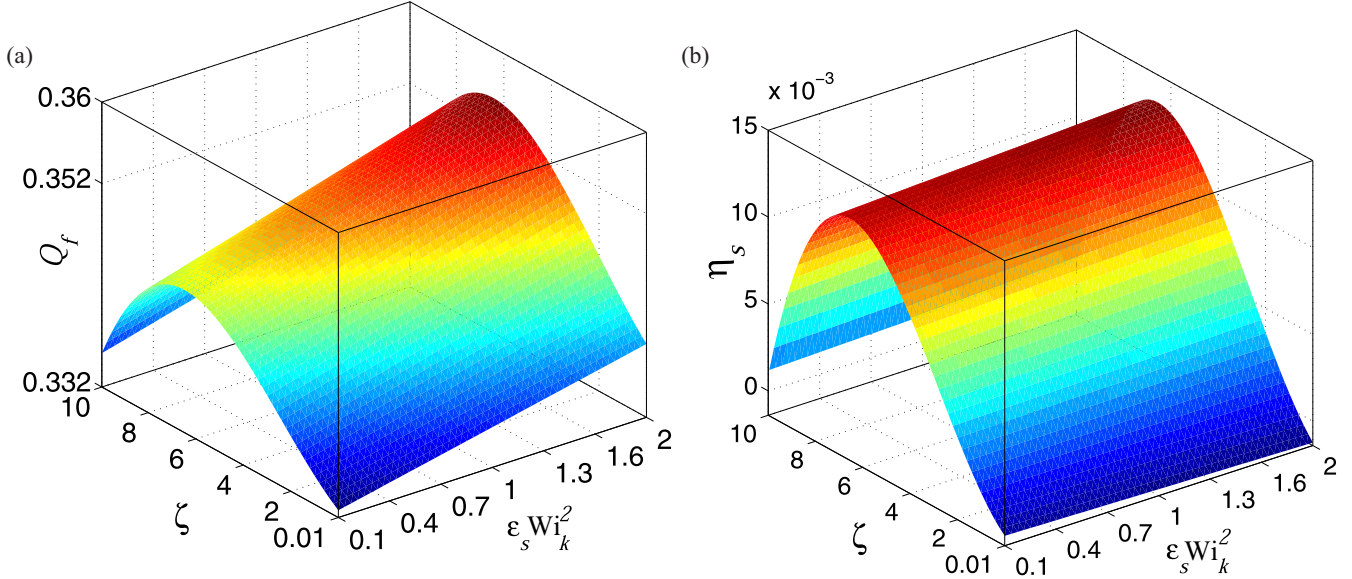


FIG. 11. Variation of the (a) dimensionless volumetric flow rate (Q_f); (b) hydroelectric energy conversion efficiency (η_s), as a function of ζ and $\varepsilon_s Wi_k^2$ for constant values of the parameters $\kappa = 10$, $Du = 0$.

other higher ranges of the applied electric field, Moschopoulos *et al.* [62] proposed an empirical correlation of the optimal PDL thickness based nonlinear regression as $\delta_{PDL} = kE_{xx}^B$, where k , B , are the constant parameters. Now, in the present study, we have not considered the formation of PDL in the proposed model, making it less realistic and robust. More importantly, the hydroelectrical energy conversion efficiency, as obtained from the current theoretical model calculations without considering the formation of PDL, will overestimate the results as compared to the actual cases. Furthermore, an increase in the PDL leads to a corresponding increase in the mean velocity of the flow [62]. One may alternatively appeal to this PDL induced enhancement in mean velocity directly to the corresponding alternation in the induced streaming potential field, which will eventually be reflected in the hydroelectrical energy conversion efficiency.

IV. CONCLUDING REMARKS

In this study, we have explored the streaming potential mediated pressure driven electrohydrodynamic transport mechanism of Phan-Thien–Tanner fluids in a microchannel employing both analytical and semianalytical approaches. Without resorting to the conventional Debye–Hückel linearization approximation for low surface potentials ($|\zeta^*| < 26$ mV), we obtain closed form analytical solutions for the dimensionless electrostatic potential distribution, velocity profile, and volumetric flow rates by utilizing full scale solution for the Poisson-Boltzmann equation. Corresponding sets of analytical formulas are also derived with the Debye–Hückel approximation. With detailed examinations of the influences of various governing electrokinetic and fluid rheological parameters, the following important conclusions are obtained from the present research:

(i) An intensification of the degree of surface charging yields the induced streaming potential field to obey a bell-

shaped distribution afterward, an asymptotic drift beyond the values of $\zeta > 6$.

(ii) The enhanced shear thinning characteristics of the fluid cause the induced streaming potential field to augment linearly with increasing viscoelastic set $\varepsilon_s Wi_k^2$, and at $\kappa = 10, 40$, are expressed by the following relationships: $E_{\kappa=10} = 4 \times 10^{-4} \varepsilon_s Wi_k^2 + 0.0134$, $E_{\kappa=40} = 10^{-6} \varepsilon_s Wi_k^2 + 0.0014$. On the other hand, enhancing the Stern layer conductivity shows a dramatic reduction in E .

(iii) The flow field is amplified by increasing the degree of surface charging. A similar trend is followed when the dimensionless viscoelastic parameter set $\varepsilon_s Wi_k^2$ is augmented. Furthermore, the flow velocity loses its strength when the dimensionless parameter κ is increased.

(iv) The dependence of polymeric normal and shear stress components with ζ is affirmed to govern by the corresponding variation in the induced streaming potential field with dimensionless surface charging. Revealing both τ_{xx} and τ_{xy} increases with increasing ζ . We further found that increasing $\varepsilon_s Wi_k^2$ leads to significant enhancement in normal stress components. In contrast, a very weak influence is witnessed on the shear stress component.

(v) The dimensionless shear viscosity drops with augmenting ζ up to a threshold limit of $\zeta = 6$, beyond $\zeta > 6$, μ_s increases with incrementing ζ , whereas the average shear viscosity follows an opposing trend with modulating electrohydrodynamic parameters and follows an inverted parabolic shape with increasing ζ .

(vi) Until the peak saturation limit in the neighborhood of $\zeta \sim 6$, a giant augmentation in the hydroelectric energy conversion efficiency is achievable. On the other hand, in the range of $6 < \zeta \leq 10$, the energy conversion efficiency decays with increasing ζ . The hydroelectric energy conversion efficiency linearly amplifies with augmenting $\varepsilon_s Wi_k^2$. The dependence of η_s with $\varepsilon_s Wi_k^2$ at $\kappa = 10, 40$, are expressed by the following relationships: $[\eta_s]_{\kappa=10} = 6 \times 10^{-4} \varepsilon_s Wi_k^2 + 0.0128$, $[\eta_s]_{\kappa=40} = 2 \times 10^{-7} \varepsilon_s Wi_k^2 + 8 \times 10^{-5}$.

(vii) For particular optimal combinations of $(\zeta, \varepsilon_s Wi_k^2)$, maximization in flow rates and hydroelectric energy conversion efficiency is achievable. The optimal regime for maximal flow rate falls at specific combinations of $\zeta \sim 6$, $\varepsilon_s Wi_k^2 \sim 2$, whereas the corresponding regime for the energy conversion efficiency falls within the narrow band of zeta potentials.

The analytical and semianalytical results presented in this research are anticipated to provide a profound insight on the employability of viscoelastic fluids in microfluidic devices. We believe that the present study will act as a predecessor for the design and syntheses of modern generation biomedical lab-on-a-cell and lab-on-a-chip devices, micromechanical smart sensors, actuators, etc. On the other hand, the analytical solutions may be used as a basis of benchmark for validation of experimental, numerical data on the electrohydrodynamic transport of the PTT fluids in a microchannel for a wide range of zeta potentials.

APPENDIX A: INFLUENCE OF STERIC EFFECT

Here we investigate the implications of the steric effect on the streaming potential mediated flow of PTT fluids in a microchannel. It is essential to mention in this context that although the Poisson-Boltzmann equation provides a more realistic representation of the electrochemical potential than the Debye-Hückel model, it also assumes ions as pointlike particles thus enabling the local ion volume fractions to exceed by orders of magnitude the maximum allowed coverage of the charged surface [74]. To remedy this inconsistency, one should include excluded-volume (or steric) effects [62,75]. The modified space-charge model by incorporating the ionic flux density in the transport of species equation forms the theoretical model describing volume (or steric) effects of the ions, expressed as [49,76]

$$\vec{J}_i = \vec{U} n_i - D_i n_i \vec{\nabla} \left(\ln a_i + \frac{z_i e \Psi}{k_B T} \right), \quad (\text{A1})$$

where n_i is the number density, D_i is the diffusivity, and z_i is the valency of the i th ionic species, respectively. The activity a_i of i th ionic species is expressed as $a_i = \frac{n_i/n_{\text{ref}}}{1 - \gamma \sum_i n_i/n_{\text{ref}}}$ [49]. Here, n_{ref} is the reference ionic number density and is treated as n_0 in the current study. The parameter γ is the steric factor or the partial molal volume fraction of the ions, which is mainly included within the ionic flux density through the activity coefficient a_i . Now, the ionic species conservation equation describes the transport characteristics of individual ions through the microchannel under steady-state condition, written as [49,76]

$$\vec{\nabla} \cdot \vec{J}_i = 0. \quad (\text{A2})$$

Without the presence of the ionic advective transport, Eq. (A2) yields [49,76]

$$\ln a_i + \frac{z_i e \Psi}{k_B T} = \text{const.} \quad (\text{A3})$$

Now, for a $z^+ : z^-$ symmetric electrolyte, an equilibrium condition prevails between the microchannel and its linking reservoir, which allows us to write $n_+ = n_- = n_0$. Therefore

the ionic number density takes the following form:

$$n_{\pm} = n_0 \frac{\exp\left(\mp \frac{e z \Psi}{k_B T}\right)}{1 + 2\gamma \left\{ \cosh\left(\frac{e z \Psi}{k_B T}\right) - 1 \right\}}. \quad (\text{A4})$$

Accordingly, the net charge density per unit fluid volume is given by

$$\rho_e = e (z_+ n_+ - z_- n_-) = e z (n_+ - n_-) \quad (\text{A5})$$

Next, if we substitute Eq. (A4) in Eq. (A5) and use Eq. (2), we obtain the Poisson-Boltzmann equation considering the steric effect, in dimensionless form, as [76]

$$\frac{d^2 \psi}{dy^2} = \kappa^2 \frac{\sinh(\psi)}{1 + 4\gamma \sinh^2(\psi/2)}. \quad (\text{A6})$$

The dimensionless set of boundary conditions, as supplemented with Eq. (A6), is [76] $[\psi]_{y=\pm 1} = \zeta$ and $[d\psi/dy]_{y=0} = 0$. Now, for obtaining the dimensionless velocity distribution, we have employed the nondimensional form of governing momentum equation, Eq. (19), with the pertinent boundary conditions as detailed in Sec. IID. In this context, it is essential to mention here that the term $d\psi/dy$ in Eq. (19) should be obtained from the solution to Eq. (A6). Finally, the closure relationship for the unknown nondimensional streaming potential field E in Eq. (19) can be found by the following criteria for the dimensionless form of electroneutrality considering the steric effect:

$$\int_0^1 \frac{\sinh(\psi)}{1 + 4\gamma \sinh^2(\psi/2)} u(y) dy - \frac{\alpha E}{\zeta} \left[\int_0^1 \frac{\cosh(\psi)}{1 + 4\gamma \sinh^2(\psi/2)} dy + \text{Du} \right] = 0. \quad (\text{A7})$$

One important thing to note here is that we have used the same set of scaling parameters as given in Sec. II for casting the governing equations, Eqs. (A6), (A7), and (19), in dimensionless form. Now, for obtaining a solution to the velocity and induced streaming potential field corresponding to the present physical situation, we have used the finite volume based numerical method [77]. The solution strategy adopted for the nonlinear sets of Eqs. (A6), (A7), and (19), are as follows: We start by solving Eq. (A6) along with the prescribed boundary conditions by employing the TDMA method [77]. With the known values of EDL potential, we then assume a guess value of E and solve Eq. (19) with the pertinent boundary conditions. Next, we check for the electroneutrality as prescribed by Eq. (A7) and update the value of E and rerun this iteration steps until convergence.

To bring out the effect of the steric factor on the induced streaming potential field, we plot the variations in E with γ in Fig. 12(a) for $\kappa = 10, 20, 30$, for the relevant parameters given in the figure caption. From Fig. 12(a) it is evident that the induced streaming potential field progressively increases with increasing γ . We explain the apparent reason for this enhancement in E by looking into the nature of γ on the electrokinetic characteristics. Increasing the steric factor increases the finite size of the ion and thereby imposes a constraint on the ionic packing nearer to the channel walls. As a consequence, lower numbers of counterions are attached to the charged substrate within the EDL region. Therefore,

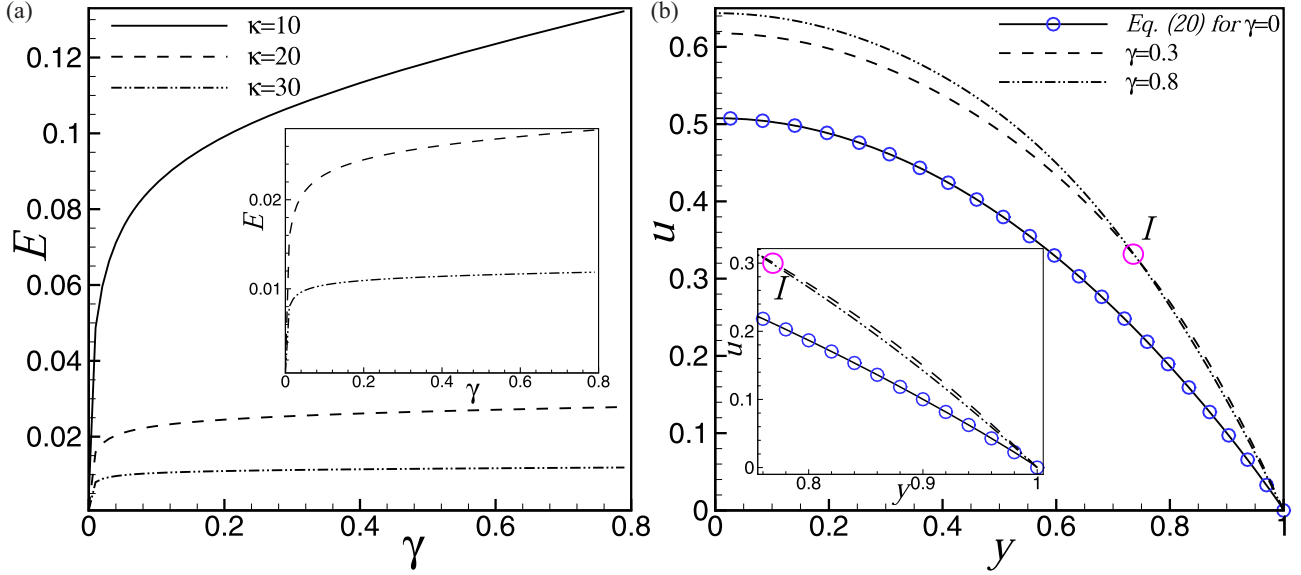


FIG. 12. (a) Variation of the dimensionless induced streaming potential (E) with γ for different κ at $\zeta = 10$, $Du = 0$, $\varepsilon_s Wi_k^2 = 1$. (b) Variation of the dimensionless velocity (u) along the cross section of the confinement (y) for different γ at $\zeta = 10$, $Du = 0$, $\kappa = 10$, $\varepsilon_s Wi_k^2 = 1$.

the zone of the net electric charge stretched to the higher bulk velocity locations and thus increasing numbers of free counterions in the flow. Subsequently, there is a corresponding intensification in the accumulation of the counterions at the channel exit, and this finally leads to higher streaming potential magnitude [76,78]. We also note that higher values of κ yield a corresponding decay in E magnitudes, which is as noted previously with the observations discussed concerning Fig. 3.

In Fig. 12(b), we plot the variation of dimensionless velocity across the microchannel as a function of the steric factor for the parameters given in the figure caption. Figure 12(b) shows that as the steric factor is increased, there is a continuous enhancement in the fluid velocity. This increase in fluid velocity is attributed to the simultaneous enhancement in the induced streaming potential field (E), which concomitantly increases the shear rate ($\bar{\gamma}$), as from Eq. (31) it can be deduced that $\bar{\gamma} \propto E^3$. The resulting consequence yields a continuous reduction in the shear viscosity (μ_s), as Eq. (32) allows us to write $\mu_s \propto 1/\bar{\gamma}$, which explains the gradual reduction in the effective flow resistance thereby increasing the fluid velocity magnitude at higher γ values. On the other hand, in the EDL region, we observe an opposite trend in velocity distribution away from the channel wall for increasing γ . This near-wall velocity distribution essentially brings about an emergence of the intersectional point I towards the channel core. The physical explanation behind this observation is as follows. At higher γ factors, the counterion concentration nearer the vicinity of the wall encompassing the EDL region reduces, leading to the decrement in the flow velocity due to reduced electrokinetic forcing. Perhaps, to satisfy the conservation of mass in the flow, it further increases towards the channel core thereby originating the intersectional point I . It is worth mentioning that consideration of ionic species as point charges ($\gamma = 0$) instead of being finite sized, we recover the analytical solution for the velocity distribution given by

Eq. (20). The agreement between the velocity profiles obtained by our numerical result to that of an analytical solution establishes the validity of the numerical method employed.

To elucidate the influence of the steric parameter on polymeric stress components, we plot the dimensionless normal (τ_{xx}) and shear stress (τ_{xy}) components [given by Eq. (30)] across the microchannel (y) in Fig. 13 for the parameters given in the caption. From the figure, we observe that as the value of γ increases, the magnitude of the stress components increases. An increase in the stress components is associated with the corresponding enhancement in the streaming potential magnitudes with augmenting γ , because $\tau_{xx} \propto E^2$ and $\tau_{xy} \propto E$ [see Eq. (30)]. However, nearer the channel walls, increasing γ yields a reverse trend in the magnitude of the stress components. As a result, there is an emergence of the intersectional point I on the variations of τ_{xx} , τ_{xy} , with y . We explain this phenomenon by the fact that increasing γ brings about a progressive reduction in the velocity gradient at the near-wall region (see Fig. 12). Accordingly, there is a consequent decrement in the stress component magnitudes with incrementing γ . We further note that the assumption of ionic species as the point charges ($\gamma = 0$) recovers the analytical solutions of the stress components given by Eq. (30).

In Fig. 14(a), we plot the variation of the dimensionless shear viscosity μ_s [expressed by Eq. (32)] across the microchannel (y) as a function of the steric factor γ for parameters given in the figure caption. Figure 14(a) indicates that for increasing the steric parameter, the magnitude of μ_s is progressively smaller than that of the case with $\gamma = 0$, which corresponds to the point charge situation. This reduction in μ_s is attributed to the corresponding enhancement in the induced streaming potential magnitude with increasing γ since the functional dependence between them obeys an inverse relationship, which can be expressed from Eq. (32) as $\mu_s \propto 1/E^2$. However, this trend reverses in the EDL region nearer the channel wall, because of considerable proportional

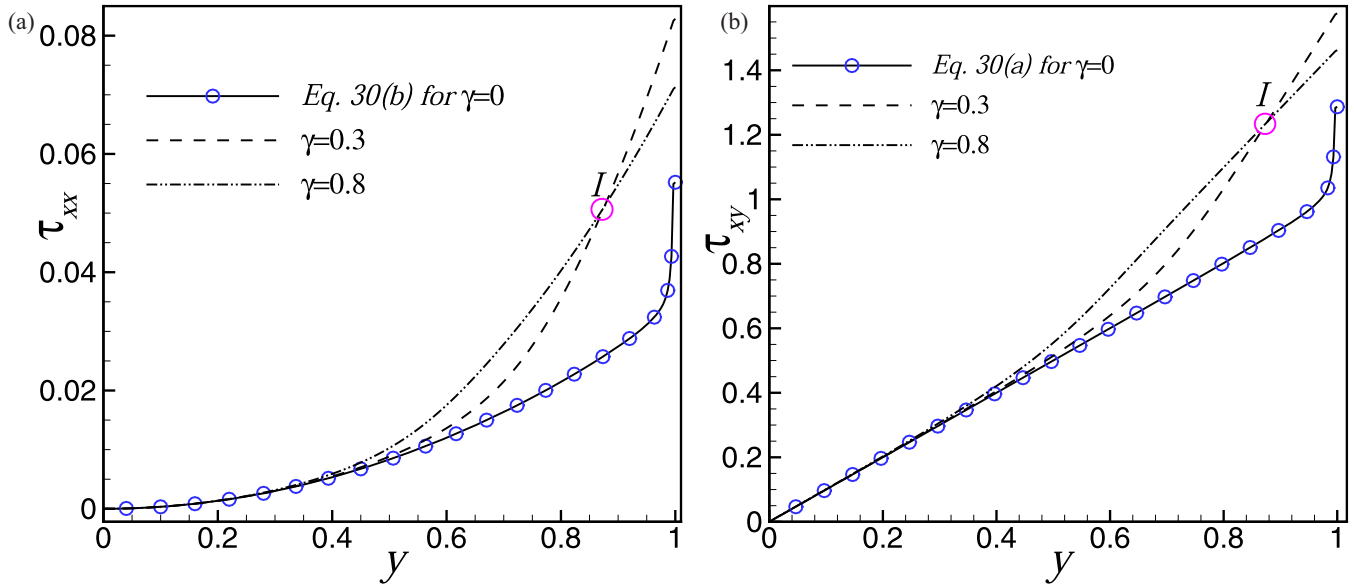


FIG. 13. Variation of the dimensionless (a) normal stress (τ_{xx}) and (b) shear stress (τ_{xy}) components along the cross section of the confinement (y) for different γ at $\zeta = 10$, $Du = 0$, $\kappa = 10$, $\epsilon_s Wi_k^2 = 1$.

reduction in the velocity gradients. In effect, appearances of the intersection point I on the variations of the $\mu_s - y$ curve. Again, we recover the analytical solution of μ_s given by Eq. (32) from the numerical results at $\gamma = 0$.

In Fig. 14(b), we show the variations in energy conversion efficiency, η_s , with γ , corresponding to the cases displayed in Fig. 12(a). A closer inspection of Fig. 14(b) reveals that the energy conversion efficiency increases with increasing the steric parameter γ , which essentially follows the trend in the induced streaming potential field [Fig. 12(a)]. This increase in the hydroelectrical energy conversion efficiency with increments in the steric parameter is due to the proportionate enhancement of the induced streaming potential field. Thus,

we see that by incorporation of finite size effects of ions, the actual energy conversion efficiency is higher than that of cases when the ionic species are considered to be as point charge. Furthermore, we again observe that increasing values of κ leads to a gradual reduction in energy conversion efficiency.

APPENDIX B: EFFECT OF THE SOLVENT VISCOSITY CONTRIBUTION

In general, for the flow of biofluids, zero-shear-rate viscosity is of the order of $O(10^{-3} - 10^{-2})$, where the viscosity of an aquatic solvent is approximately $\sim 10^{-3}$ [41,62]. In that situation, apparently, the solvent viscosity contribution is not

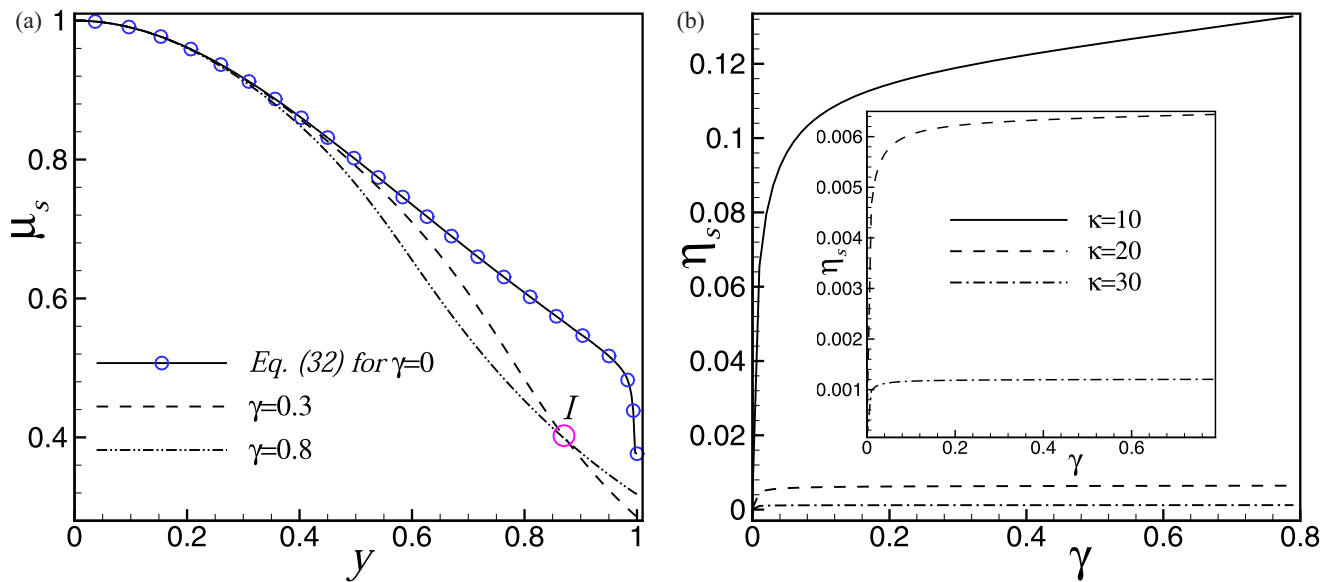


FIG. 14. (a) Variation of the dimensionless shear viscosity (μ_s) along the cross section of the confinement (y) for different γ at $\zeta = 10$, $Du = 0$, $\kappa = 10$, $\epsilon_s Wi_k^2 = 1$. (b) Variation of the hydroelectrical energy conversion efficiency (η_s) with γ for different κ at $\zeta = 10$, $Du = 0$, $\epsilon_s Wi_k^2 = 1$.

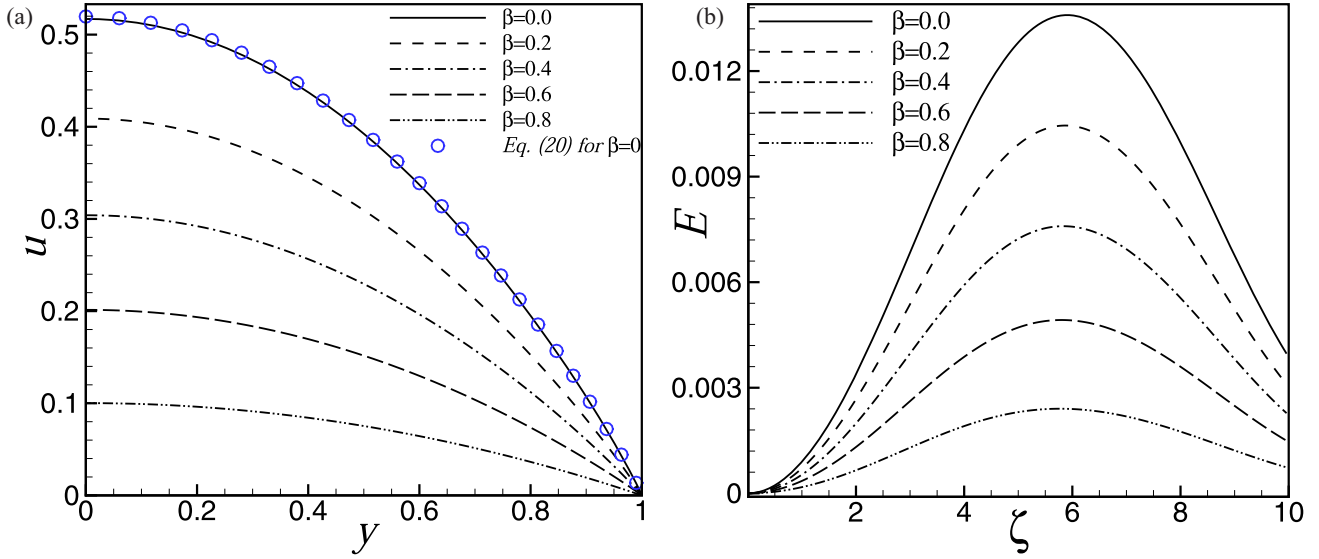


FIG. 15. (a) Variation of the dimensionless velocity (u) along the cross section of the confinement (y) for different β at $\zeta = 6$, $Du = 0$, $\kappa = 10$, $\varepsilon_s Wi_k^2 = 1$. (b) Variation of the dimensionless induced streaming potential (E) with ζ for different β at $\kappa = 10$, $Du = 0$, $\varepsilon_s Wi_k^2 = 1$.

negligible. When the contribution of the solvent viscosity is considered, the term $\eta_{\text{eff}} \nabla^2 \vec{U}$ appearing in the governing equation Eq. (7b) is taken into consideration. In this case, by employing the same set of scaling parameters for length (a), velocity (U_{ref}), and streaming potential (E_{ref}) as given in Sec. II, we can recast the corresponding dimensionless form of the governing equation for the flow inside the microchannel as

$$\frac{du}{dy} = \left\{ \frac{E}{\zeta} \frac{d\psi}{dy} - y - \left(\frac{\beta}{1-\beta} \right) \frac{du}{dy} \right\} + \frac{2\varepsilon_s Wi_k^2}{\kappa^2} \left\{ \frac{E}{\zeta} \frac{d\psi}{dy} - y - \left(\frac{\beta}{1-\beta} \right) \frac{du}{dy} \right\}^3, \quad (\text{B1})$$

where $\beta = \eta_{\text{eff}}/(\eta + \eta_{\text{eff}})$ represents the viscosity ratio [41]. The pertinent boundary conditions for Eq. (B1) are symmetry at the channel centerline and no-slip at the walls, $u(y)|_{y=\pm 1} = 0$. As evident in Eq. (B1), the dimensionless streaming potential E is an unknown parameter. That can

again be obtained by using the electroneutrality constraint expressed in the dimensionless form by Eq. (23); perhaps the dimensionless velocity $u(y)$ obtained from Eq. (B1) also has a functional relationship with E . Furthermore, Eq. (B1) necessitates the information of EDL potential distribution, which is obtained by the full analytic solution to the Poisson-Boltzmann equation given by Eq. (5). We have used a numerical technique to obtain the velocity and streaming potential distributions for the physical situation described above. Towards this, we employ the following numerical formalism: By assuming a guess value of E , we solve Eq. (B1) along with the appropriate boundary conditions iteratively by the finite volume method [77]. We then check for the electroneutrality as given by Eq. (23) and update the value of E . We repeat these iteration steps until convergence.

Employing similar procedures as described in the previous section, we can write the expressions for dimensionless components of normal and shear stress as

$$\tau_{xx} = \frac{\tau_{XX}}{\eta U_{\text{ref}} \bar{\kappa}} = 2 \frac{Wi_k}{\kappa^2} \left[y - \frac{4E\kappa p e^{\kappa(y-1)}}{\zeta \{1 - p^2 e^{2\kappa(y-1)}\}} + \left(\frac{\beta}{1-\beta} \right) \frac{du}{dy} \right]^2, \quad (\text{B2})$$

$$\tau_{xy} = y - \frac{4E\kappa p e^{\kappa(y-1)}}{\zeta \{1 - p^2 e^{2\kappa(y-1)}\}} + \left(\frac{\beta}{1-\beta} \right) \frac{du}{dy}. \quad (\text{B3})$$

Furthermore, the dimensionless expression for the shear rate becomes

$$\bar{\Upsilon} = \frac{\bar{\chi}}{(-U_{\text{ref}}/a)} = \left[y - \frac{4E\kappa p e^{\kappa(y-1)}}{\zeta \{1 - p^2 e^{2\kappa(y-1)}\}} + \left(\frac{\beta}{1-\beta} \right) \frac{du}{dy} \right] \times \left[1 + \frac{2\varepsilon_s Wi_k^2}{\kappa^2} \left\{ y - \frac{4E\kappa p e^{\kappa(y-1)}}{\zeta \{1 - p^2 e^{2\kappa(y-1)}\}} + \left(\frac{\beta}{1-\beta} \right) \frac{du}{dy} \right\}^2 \right]. \quad (\text{B4})$$

Finally, the nondimensional form of shear viscosity profile, $\mu_s = \tau_{xy}/\bar{\Upsilon}$, can be expressed as

$$\mu_s = \left[1 + \frac{2\varepsilon_s Wi_k^2}{\kappa^2} \left\{ y - \frac{4E\kappa p e^{\kappa(y-1)}}{\zeta \{1 - p^2 e^{2\kappa(y-1)}\}} + \left(\frac{\beta}{1-\beta} \right) \frac{du}{dy} \right\}^2 \right]^{-1}. \quad (\text{B5})$$

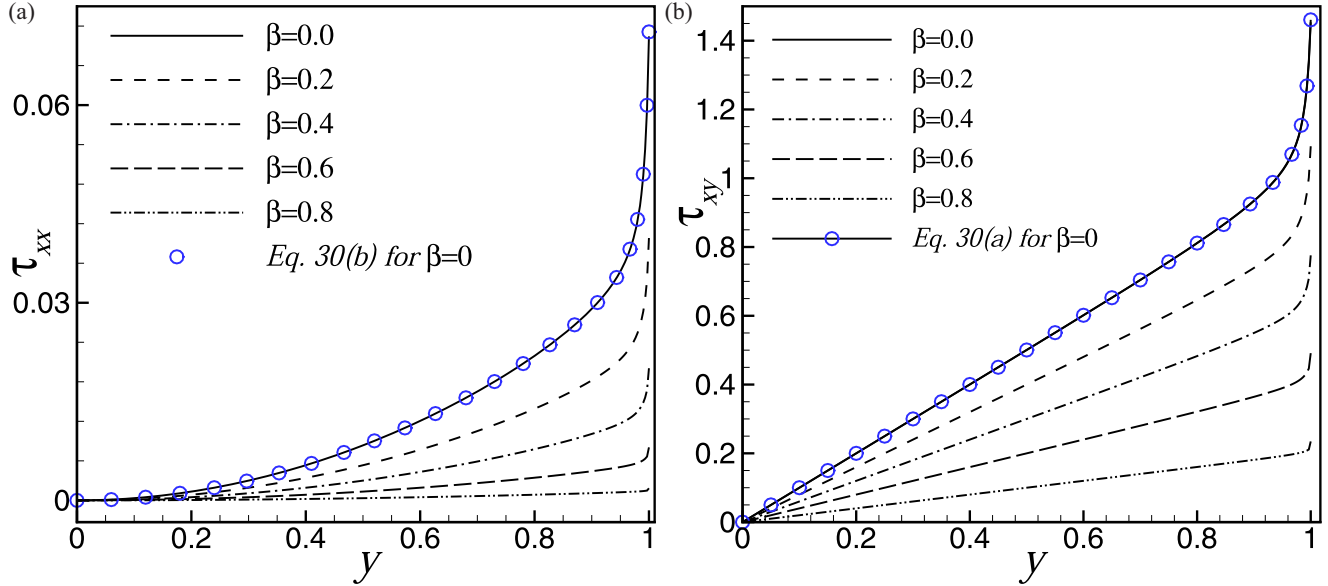


FIG. 16. Variation of the dimensionless (a) normal stress (τ_{xx}) and (b) shear stress (τ_{xy}) components along the cross section of the confinement (y) for different β at $\zeta = 6$, $Du = 0$, $\kappa = 10$, $\varepsilon_s Wi_k^2 = 1$.

To investigate the influence of β on the dimensionless velocity profile, we plot the variation of $u(y)$ along the cross section of the microchannel (y) in Fig. 15(a) for the parameters given in the figure caption. Figure 15(a) depicts that as the viscosity ratio (β) is increased or, in other words, a reduction in polymeric contribution, there is a gradual suppression in the dimensionless velocity profiles. The trend of variation of $u(y)$ with β is similar to the one reported by Cruz *et al.* [79] for fully developed pressure-driven laminar pipe flow of the PTT fluids, where an increase in the concentration of the viscoelastic polymer (reduction in the values of β) was reported, defined by $C_0 = \eta/\eta_{\text{eff}} = (1 - \beta)/\beta$, in consequence of triggering shear-thinning influences increasing the fluid velocity. A slightly different type of behavior of fluid velocity with β was reported for the PTT fluids by Ferrás *et al.* [41] for pure electro-osmotic flow in a microchannel, where they [41] adopted different normalization methods. However, in the present research, in order to maintain consistency with the results obtained in the analytical calculations, we have used the same normalization technique for velocity, which is solely normalized based on polymeric viscosity (η) and pressure drop, $u = U/U_{\text{ref}}$, and $U_{\text{ref}} = -(a^2/\eta)(dp/dX)$. An interesting point to observe from Fig. 15(a) is that for $\beta \rightarrow 0$, the analytical solution, as given by Eq. (20), is recovered, indicated by blue circular markers. This result also supports the validity of the present numerical model with the analytical solutions in a good agreement.

In Fig. 15(b), we show the variation of the dimensionless induced streaming potential (E) field with ζ for different values of β and the other parameters indicated in the caption. As observed from this figure, higher values of β induces a lower magnitude of E . This is attributed to the fact that for a given value of ζ , a higher β leads to a lower magnitude of velocity distribution across the channel [Fig. 15(a)]. As a consequence, for a given ionic concentration in the EDL (fixed by the value of ζ), there is a reduction in the advective strength of the

ionic species. That, in turn, lowers the back electrokinetic strength. Thus, a lesser magnitude of the electric potential is adequate to balance the streaming current for satisfying electroneutrality. The overall effects culminate in lowering the induced streaming potential field.

Now, we examine the influence of β on the stress components, for which we plot the dimensionless normal (τ_{xx}) and shear stress (τ_{xy}) components across the microchannel (y) in Fig. 16 for the parameters indicated in the figure caption. The general observation from Fig. 16 is that both the normal and shear stress components decay with an augmentation in the viscosity ratio, signifying lower polymeric concentration. The reason behind this trend is a progressive decrement in the streaming potential magnitude with increasing β , since $\tau_{xx} \propto E^2$ and $\tau_{xy} \propto E$. It is worth mentioning here that the functional dependence of stress components with β is in line with the observations reported by Cruz *et al.* [79]. In the limit of $\beta \rightarrow 0$, variations in the normal and shear stress components depicted in Fig. 16 recover the analytical solutions given by Eqs. (30b) and (30a), respectively, illustrated by blue circular markers.

Next, we investigate how the nonzero values of the solvent viscosity influence the shear viscosity function of the PTT model given by Eq. (B5). Accordingly, in Fig. 17(a) we plot the variation of the nondimensional shear viscosity μ_s across the microchannel (y) for parametric variations in β . The other physical parameters are mentioned in the figure caption. An important thing to mention here is that in a region of more significant shear rates, μ_s turns into restricted from below by η_{eff} for nonzero values of β [79]. Thus, the functional distribution of μ_s will tend to uniformity across the microchannel at higher β values. Such dependencies are very much visible from Fig. 17(a), where we see that μ_s intensifies with increasing the magnitudes of β and finally tends towards uniformity at higher β values. This observation is in line with the trend reported in Cruz

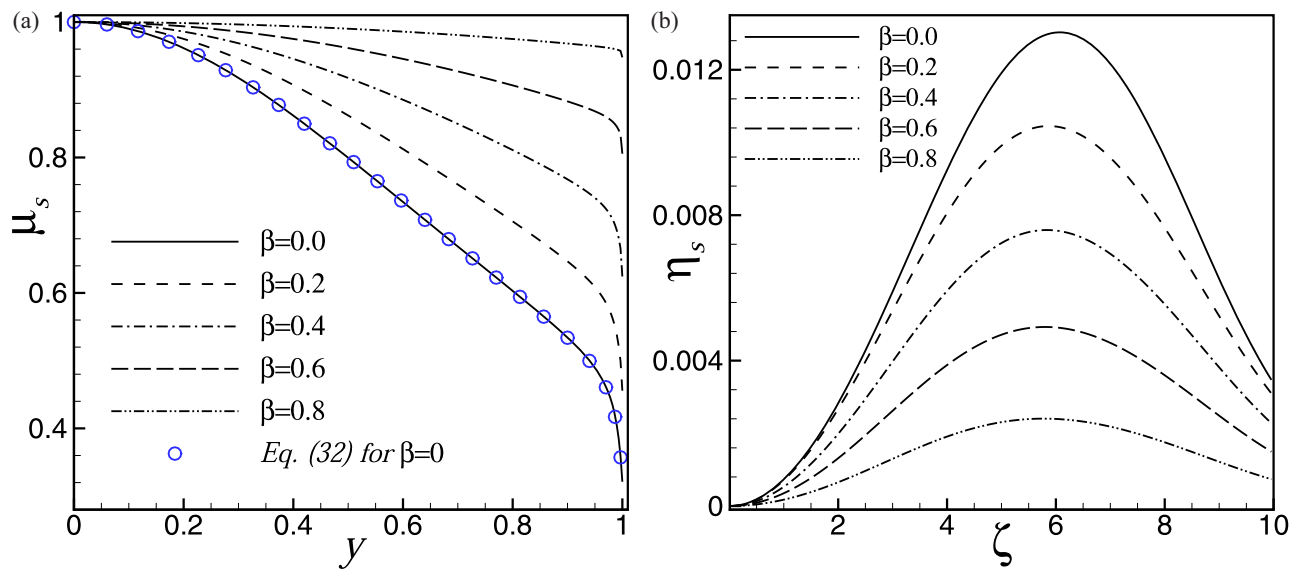


FIG. 17. (a) Variation of the dimensionless shear viscosity (μ_s) along the cross section of the confinement (y) for different β at $\zeta = 6$, $Du = 0$, $\kappa = 10$, $\varepsilon_s Wi_k^2 = 1$. (b) Variation of the hydroelectrical energy conversion efficiency (η_s) with ζ for different β at $\kappa = 10$, $Du = 0$, $\varepsilon_s Wi_k^2 = 1$.

et al. [79]. Again, we notice that the analytical solution for shear viscosity given by Eq. (32) recovered in the limit of $\beta \rightarrow 0$.

We now demonstrate the effect of β on the hydroelectrical energy conversion efficiency η_s . To portray this, in Fig. 17(b), we plot the variation of η_s as a function of ζ for various β . The other relevant parameters are mentioned in the figure caption. It is evident from Fig. 17(b) that for higher values of

β , there occurs a gradual decrement in η_s . The reduction in the induced streaming potential field with increasing β is a plausible reason for the steady decrement in the hydroelectrical energy conversion efficiency. Thus, we can proclaim that the incorporation of solvent viscosity has substantial consequences in regulating actual hydroelectric energy conversion efficiency for such streaming potential mediated flows of PTT fluids in a microchannel.

-
- [1] R. J. Hunter, *Zeta Potential in Colloid Science: Principles and Applications* (Academic, London, 1981).
- [2] R. F. Probstein, *Physicochemical Hydrodynamics* (Wiley, New York, 1994).
- [3] P. Goswami and S. Chakraborty, *Langmuir* **26**, 581 (2010).
- [4] F. Munshi and S. Chakraborty, *Phys. Fluids* **21**, 122003 (2009).
- [5] A. Bandopadhyay and S. Chakraborty, *Langmuir* **27**, 12243 (2011).
- [6] A. Bandopadhyay and S. Chakraborty, *Appl. Phys. Lett.* **101**, 043905 (2012).
- [7] H. Chang and L. Y. Yeo, *Electrokinetically-Driven Microfluidics and Nanofluidics* (Cambridge University Press, Cambridge, UK, 2009).
- [8] S. Das, T. Das, and S. Chakraborty, *Sens. Actuators, B* **114**, 957 (2006).
- [9] S. Das and S. Chakraborty, *AIChE J.* **53**, 1086 (2007).
- [10] S. Chakraborty, *J. Phys. D: Appl. Phys.* **39**, 5356 (2006).
- [11] A. Bandopadhyay, D. Tripathi, and S. Chakraborty, *Phys. Fluids* **28**, 052002 (2016).
- [12] S. Chakraborty and S. Ray, *Phys. Fluids* **20**, 083602 (2008).
- [13] A. L. Garcia, L. K. Ista, D. N. Petsev, M. J. O'Brien, P. Bisong, A. A. Mammoli, S. R. J. Brueck, and G. P. López, *Lab Chip* **5**, 1271 (2005).
- [14] I. Glasgow, J. Batton, and N. Aubry, *Lab Chip* **4**, 558 (2004).
- [15] A. S. Rathore and C. Horváth, *J. Chromatogr. A* **781**, 185 (1997).
- [16] T. Ye, N. Phan-Thien, B. C. Khoo, and C. T. Lim, *Phys. Fluids* **26**, 111902 (2014).
- [17] T. X. Ho, N. Phan-Thien, and B. C. Khoo, *Phys. Fluids* **28**, 063305 (2016).
- [18] S. Mukherjee, P. Goswami, J. Dhar, S. Dasgupta, and S. Chakraborty, *Phys. Fluids* **29**, 072002 (2017).
- [19] M. Moyers-Gonzalez, R. Owens, and J. Fang, *J. Fluid Mech.* **617**, 327 (2008).
- [20] J. G. Oldroyd, *Proc. R. Soc. London, Ser. A* **245**, 278 (1958).
- [21] H. Fam, J. T. Bryant, and M. Kontopoulou, *Biorheology* **44**, 59 (2007).
- [22] J. T. Mannion, C. H. Reccius, J. D. Cross, and H. G. Craighead, *Biophys. J.* **90**, 4538 (2006).
- [23] S. Chakraborty, *Electrophoresis* **40**, 180 (2019).
- [24] H. A. Stone, A. D. Stroock, and A. Ajdari, *Annu. Rev. Fluid Mech.* **36**, 381 (2004).
- [25] A. M. Afonso, M. A. Alves, and F. T. Pinho, *J. Non-Newtonian Fluid Mech.* **159**, 50 (2009).
- [26] J. D. Evans, J. A. Cuminato, I. L. Palhares Junior, and C. M. Oishi, *Phys. Fluids* **31**, 093101 (2019).

- [27] N. P. Thien and R. I. Tanner, *J. Non-Newtonian Fluid Mech.* **2**, 353 (1977).
- [28] J. Chakraborty, R. Dey, and S. Chakraborty, *Phys. Rev. E* **86**, 061504 (2012).
- [29] T. Ghonge, J. Chakraborty, R. Dey, and S. Chakraborty, *Phys. Rev. E* **88**, 053020 (2013).
- [30] U Ghosh and S Chakraborty, *Phys. Rev. E* **88**, 033001 (2013).
- [31] L. L. Ferrás, A. M. Afonso, M. A. Alves, J. M. Nobrega, and F. T. Pinho, *Phys. Fluids* **28**, 093102 (2016).
- [32] S. Chakraborty, *Anal. Chim. Acta* **605**, 175 (2007).
- [33] C. Zhao and C. Yang, *J. Non-Newtonian Fluid Mech.* **166**, 1076 (2012).
- [34] A. Sadeghi, H. Veisi, M. Hassan Saidi, and A. Asghar Mozafari, *ASME J. Heat Transfer* **135**, 021706 (2013).
- [35] A. M. Afonso, M. A. Alves, and F. T. Pinho, *J. Colloid Interface Sci.* **395**, 277 (2013).
- [36] A. M. Afonso, M. A. Alves, and F. T. Pinho, *J. Eng. Math.* **71**, 15 (2010).
- [37] L. L. Ferrás, A. M. Afonso, M. A. Alves, J. M. Nóbrega, and F. T. Pinho, *J. Colloid Interface Sci.* **420**, 152 (2014).
- [38] P.C. Sousa, F.T. Pinho, M.S.N. Oliveira, and M.A. Alves, *J. Non-Newtonian Fluid Mech.* **165**, 652 (2010).
- [39] J. Escandón, O. Bautista, and F. Méndez, *Energy* **55**, 486 (2013).
- [40] J. Escandón, F. Santiago, O. Bautista, and F. Mendez, *Int. J. Thermal Sc.* **86**, 246 (2014).
- [41] L. L. Ferrás, A. S. Cavadas, P. R. Resende, A. M. Afonso, and F. T. Pinho, *J. Non-Newt. Fluid Mech.* **259**, 125 (2018).
- [42] A. M. Afonso, L. L. Ferrás, J. M. Nóbrega, M. A. Alves, and F. T. Pinho, *Microfluid. Nanofluid.* **16**, 1131 (2014).
- [43] P. M. Coelho, M. A. Alves, and F. T. Pinho, *Microfluid. Nanofluid.* **12**, 431 (2012).
- [44] S. Sarkar, S. Ganguly, and P. Dutta, *Chem. Eng. Sci.* **171**, 391 (2017).
- [45] S. Sarkar, S. Ganguly, and S. Chakraborty, *Microfluid. Nanofluid.* **21**, 56 (2017).
- [46] S. Sarkar and S. Ganguly, *J. Non-Newtonian Fluid Mech.* **250**, 18 (2017).
- [47] A. Bandopadhyay and S. Chakraborty, *Phys. Rev. E* **85**, 056302 (2012).
- [48] A. Bandopadhyay and S. Chakraborty, *Langmuir* **28**, 17552 (2012).
- [49] A. Bandopadhyay, S. S. Hossain, and S. Chakraborty, *Langmuir* **30**, 7251 (2014).
- [50] Z. Ding, Y. Jian, L. Wang, and L. Yang, *Phys. Fluids* **29**, 082008 (2017).
- [51] A. Bandopadhyay, U. Ghosh, and S. Chakraborty, *Phys. Rev. E* **89**, 053024 (2014).
- [52] S. Chakraborty, *Phys. Rev. Lett.* **100**, 097801 (2008).
- [53] V. Tandon, S. K. Bhagavatula, W. C. Nelson, and B. J. Kirby, *Electrophoresis* **29**, 1092 (2008).
- [54] H. Bruus, *Theoretical Microfluidics* (Oxford University Press, 2008).
- [55] S. G. Hatzikiriakos, *Int. Polym. Process.* **8**, 135 (1993).
- [56] S. Sarkar, S. Ganguly, and P. Dutta, *Int. J. Heat Mass Transfer* **100**, 451 (2016).
- [57] C. Zhao and C. Yang, *Adv. Colloid Interface Sci.* **201–202**, 94 (2013).
- [58] N. Phan-Thien, *J. Rheol.* **22**, 259 (1978).
- [59] A. Bandopadhyay and S. Chakraborty, *Phys. Chem. Chem. Phys.* **17**, 7282 (2015).
- [60] Y. Jian, F. Li, Y. Liu, L. Chang, Q. Liu, and L. Yang, *Colloids Surf. B: Biointerfaces* **156**, 405 (2017).
- [61] A. Sailaja, B. Srinivas, and I. Sreedhar, *J. Mech.* **35**, 537 (2019).
- [62] P. Moschopoulos, Y. Dimakopoulos, and J. Tsamopoulos, *J. Colloid Interface Sci.* **563**, 381 (2020).
- [63] L. G. Leal, *Advanced Transport Phenomena: Fluid Mechanics and Convective Transport Processes* (Cambridge University Press, Cambridge, UK, 2007).
- [64] P. K. Kundu and I. M. Cohen, *Fluid Mechanics* (Elsevier, New York, 2008).
- [65] S. Dhinakaran, A. M. Afonso, M. A. Alves, and F. T. Pinho, *J. Colloid Interface Sci.* **344**, 513 (2010).
- [66] J. Yang and D. Y. Kwok, *Langmuir* **19**, 1047 (2003).
- [67] U. Ghosh and S. Chakraborty, *Phys. Fluids* **27**, 062004 (2015).
- [68] R. J. Hunter, *Foundation of Colloid Science* (Oxford University Press, New York, 2001).
- [69] T. Yamada, C. Hong, O. J. Gregory, and M. Faghri, *Microfluid. Nanofluid.* **11**, 45 (2011).
- [70] P. J. Oliveira and F. T. Pinho, *J. Fluid Mech.* **387**, 271 (1999).
- [71] M. A. Alves, F. T. Pinho, and P. J. Oliveira, *J. Non-Newtonian Fluid Mech.* **101**, 55 (2001).
- [72] S. J. Park, A. Shakya, and J. T. King, *Proc. Natl. Acad. Sci. U. S. A.* **116**, 16256 (2019).
- [73] Y. Huang, J. Chen, T. Wong, and J.-L. Liow, *Soft Matter.* **12**, 6206 (2016).
- [74] J. Lyklema, *Solid-Liquid Interfaces, Fundamentals of Interface and Colloid Science Vol. II* (Academic, San Diego, CA, 1995).
- [75] J. J. Bikerman, *Philos. Mag. (1798–1977)* **33**, 384 (1942).
- [76] A. Garai and S. Chakraborty, *Electrophoresis* **31**, 843 (2010).
- [77] S. V. Patankar, *Numerical Fluid Flow and Heat Transfer* (Taylor and Francis, New York, 2009).
- [78] A. Bandopadhyay, J. Dhar, and S. Chakraborty, *Phys. Rev. E* **88**, 033014 (2013).
- [79] D. O. A. Cruz, F. T. Pinho, and P. J. Oliveira, *J. Non-Newton. Fluid Mech.* **132**, 28 (2005).